AGU ADVANCING EARTH AND SPACE SCIENCES

Water Resources Research

RESEARCH ARTICLE
10.1029/2024WR039836

Predicting Soil Interpedal Macroporosity and Hydraulic Conductivity Dynamics: A Model for Integrating Laser-Scanned Profile Imagery With Soil Moisture Sensor Data

Daniel R. Hirmas[1], Hoori Ajami[2], Matthew G. Sena[3], Xi Zhang[4], Xiaoyang Cao[5], Bonan Li[6], Karla M. Jarecke[7], Sharon A. Billings[8], Julio C. Pachon[9], Li Li[10], Jesse B. Nippert[11], Lígia F. T. Souza[12], Alejandro N. Flores[13], and Pamela L. Sullivan[6]

[1]Department of Plant and Soil Science, Texas Tech University, Lubbock, TX, USA, [2]Department of Environmental Sciences, University of California Riverside, Riverside, CA, USA, [3]Department of Plant and Soil Sciences, University of Delaware, Newark, DE, USA, [4]Department of Biosystems Engineering & Soil Science, University of Tennessee, Knoxville, TN, USA, [5]College of Tourism, Resources and Environment, Zaozhuang University, Zaoshuang, China, [6]College of Earth, Ocean, and Atmospheric Sciences, Oregon State University, Corvallis, OR, USA, [7]Department of Geography, University of Colorado Boulder, Boulder, CO, USA, [8]Department of Ecology and Evolutionary Biology and Kansas Biological Survey & Center for Ecological Research, University of Kansas, Lawrence, KS, USA, [9]Sydney Institute of Agriculture, School of Life and Environmental Sciences, University of Sydney, Camperdown, NSW, Australia, [10]Department of Civil and Environmental Engineering, Penn State University, University Park, PA, USA, [11]Division of Biology, Kansas State University, Manhattan, KS, USA, [12]Department of Soil and Crop Sciences, Colorado State University, Fort Collins, CO, USA, [13]Department of Geosciences, Boise State University, Boise, ID, USA

Abstract The size and spatial distribution of soil structural macropores impact the infiltration, percolation, and retention of soil water. Despite the assumption often made in hydrologic flux equations that these macropores are rigid, highly structured soils can respond quickly to moisture variability-induced shrink-swell processes altering the size distribution of these pores. In this study, we use a high-resolution (180 μm) laser imaging technique to measure the average width of interpedal, planar macropores from intact cross sections and relate it to matrix water content. We also develop an expression for unsaturated hydraulic conductivity (K) that accounts for dynamic macropore geometries and propose a method for partitioning sensor soil water content data into matrix and macropore water contents. The model was applied to a soil in northeastern Kansas where soil monoliths had been imaged to quantify macropore properties and continuous water content data were collected at three depths. Model-predicted macropore width showed significant sensitivity to matrix water content resulting in changes of ∼15%–50% of maximum width over the 15-month period of record. Transient saturated hydraulic conductivity predicted from the model compared favorably to a previously developed model accounting for moisture-induced changes to structural unit porosity. Following periods of low soil moisture, infiltrating meteoric water filled highly conductive macropores increasing K by several orders of magnitude which subsequently decreased as water was absorbed into the matrix and macropores drained. This model offers a means by which to combine measurable morphological data with soil moisture sensors to monitor dynamic hydraulic properties of soils susceptible to shrink-swell processes.

Key Points:

- We develop a theory to predict changes in interpedal macroporosity from matrix soil water content
- This theory includes a method for partitioning soil moisture sensor data into matrix and macropore water content
- We explore implications of integrating sensor data with laser imagery of soil macropores to soil hydraulic conductivity

Supporting Information:

Supporting Information may be found in the online version of this article.

Correspondence to:

D. R. Hirmas,
dhirmas@ttu.edu

Citation:

Hirmas, D. R., Ajami, H., Sena, M. G., Zhang, X., Cao, X., Li, B., et al. (2025). Predicting soil interpedal macroporosity and hydraulic conductivity dynamics: A model for integrating laser-scanned profile imagery with soil moisture sensor data. *Water Resources Research*, *61*, e2024WR039836. https://doi.org/10.1029/2024WR039836

Received 30 DEC 2024
Accepted 18 JUL 2025

Author Contributions:

Conceptualization: Daniel R. Hirmas, Hoori Ajami, Xi Zhang, Xiaoyang Cao, Sharon A. Billings, Alejandro N. Flores, Pamela L. Sullivan
Data curation: Daniel R. Hirmas, Matthew G. Sena, Sharon A. Billings, Pamela L. Sullivan
Formal analysis: Daniel R. Hirmas, Bonan Li
Funding acquisition: Daniel R. Hirmas, Hoori Ajami, Sharon A. Billings, Li Li, Jesse B. Nippert, Alejandro N. Flores, Pamela L. Sullivan
Methodology: Daniel R. Hirmas, Hoori Ajami, Xi Zhang, Xiaoyang Cao, Sharon A. Billings, Alejandro N. Flores

1. Introduction

The importance of macropores have long been recognized in subsurface flow and transport problems (Beven & Germann, 1982; Jarvis, 2007). For example, although macropores account for less than 5% of the soil volume, under saturated conditions they can contribute to more than 70% of the water flow in soils (Watson & Luxmoore, 1986). However, characterizing macropore properties (shape, size and distribution) at a horizon or pedon scale has not been possible until recently, and many subsurface flow models have implemented the single-porosity approach—that is, a single-domain representation of the pore system (Arora et al., 2011).

Recent advancements in the fields of digital soil morphometrics and proximal soil sensing have opened the door to horizon- and pedon-scale mapping of soil properties—properties that previously were only generally obtainable from disturbed bulk samples (e.g., Dauer et al., 2009; Hartemink & Minasny, 2014; Hobley et al., 2018; Xu et al., 2021; Zhang & Hartemink, 2019). Among these techniques are three-dimensional laser scanning approaches that can digitally capture and quantify aspects of soil structure (Hirmas et al., 2016). One such approach is multistripe laser triangulation (MLT) scanning that has been used to quantify excavation-wall topographic

Resources: Daniel R. Hirmas
Software: Daniel R. Hirmas, Bonan Li, Julio C. Pachon
Validation: Daniel R. Hirmas, Bonan Li, Karla M. Jarecke
Visualization: Daniel R. Hirmas
Writing – original draft: Daniel R. Hirmas
Writing – review & editing: Hoori Ajami, Matthew G. Sena, Xi Zhang, Xiaoyang Cao, Karla M. Jarecke, Sharon A. Billings, Julio C. Pachon, Li Li, Jesse B. Nippert, Lígia F. T. Souza, Alejandro N. Flores, Pamela L. Sullivan

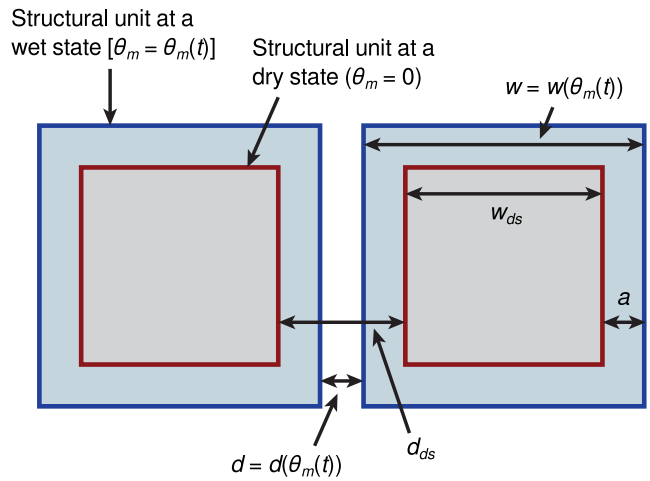

Figure 1. Idealized vertical cross-sectional diagram of two adjacent structural units represented as squares showing the structural unit boundaries at a dry state (red border) and a wet state (blue border) along with several of the variables discussed in the text and provided in Appendix A.

proxies of structural units as well as to image the distribution of interpedal macropores (Bagnall et al., 2020; Eck et al., 2013).

Imaging macropores allows their shape, size, abundance, and distribution to be quantified and used to predict field-scale soil hydraulic properties (Eck et al., 2016). One limitation of this technique, however, is that macropores are imaged when the soil is at a single, relatively dry moisture state. This is done to maximize the ability of the technique to identify and map macropores since interpedal pores will often enlarge due to shrinkage of soil structural units as the soil dries (Eck et al., 2013). Soils with sufficient clay content or whose mineralogy is influenced by 2:1 clays are particularly susceptible to shrinkage-induced changes in macropore size (Bordoloi et al., 2020). In these soils, changes in water content must be taken into account to accurately predict macropore and concomitant hydraulic property dynamics under field conditions (Bronswijk, 1988b; Chertkov & Ravina, 2001; Coppola et al., 2015). For example, water content of the soil can be underestimated when it is not allowed to influence macroporosity (Coppola et al., 2012). There is a need, then, for macropore descriptions quantified at one moisture state to be predictable at any arbitrary moisture state. Such an ability would allow soil water content sensor data to be used to understand changes in macropores and hydraulic properties in soils scanned by MLT. Furthermore, it provides a means for parameterizing dual-porosity or dual permeability models for simulating non-equilibrium flow at a pedon scale (Šimůnek & van Genuchten, 2008). This direct characterization of macropores could be beneficial to inverse modeling approaches for estimating hydraulic parameters under non-equilibrium conditions (e.g., Lewandowska et al., 2005).

The objectives of this study were, therefore, to predict dynamic porosity metrics from laser-scanned profile cross sections and soil water content sensor data. Our aim was to develop a coherent theory connecting quantified descriptions of macropores obtained from excavation walls to soil water content and to explore the implications of this theory on the estimation of saturated and unsaturated hydraulic conductivity.

2. Theory

2.1. Structural Dynamics

To integrate the MLT image-derived estimate of average macropore width (d_{ds}) measured from a soil profile at a dry state with volumetric water content (θ) of the soil, we first derive an expression for the relationship between structural unit width and macropore width. As shown in Figure 1, the distance a can be represented as:

$$a = \frac{w - w_{ds}}{2} \quad (1)$$

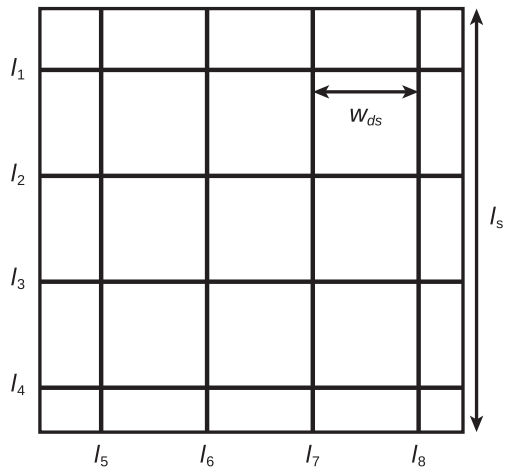

Figure 2. Diagram illustrating the relationship between the width of a structural unit (w_{ds}) assessed from MLT imagery of a monolith scanned at a dry state, the dimensions of the conceptualized equivalent-area cross section, and the number of structural units within the cross section.

where w_{ds} is the average width of a structural unit in the MLT-scanned cross section at a dry state, w is the structural unit width at a wet state, and $2a = w - w_{ds}$ is the sum of the distances that two adjacent structural units expand into the macropore at time t corresponding to a wet state. Thus, the macropore width (d) at time t can be expressed as:

$$d = d_{ds} - w + w_{ds} \tag{2}$$

In other words, the amount of reduction in d from d_{ds} is dependent on both the distance between the structural units and their size. Here d is conceptualized to change equally on each side of the structural unit. To derive an expression to estimate w_{ds} from the MLT imagery, we make the following assumptions:

1. The structural units are equidimensional and can be approximated by a cube.
2. The structural units in the horizon are all of the same size.
3. There are an integer number of structural units represented in the cross section obtained from the MLT scanner.
4. The cross section can be represented by a square of equivalent non-macroporous area (A).

The non-macroporous area can be calculated as:

$$A = A_{xs} - A_p \tag{3}$$

where A_{xs} is the area of the cross section and A_p is the total area of the macropores quantified from the MLT-derived image.

Given these assumptions, the width of a structural unit corresponding to the dry state of the MLT-scanned cross section can be illustrated as shown in Figure 2. Here, the area of the square corresponds to the cross-sectional equivalent area of the non-macroporous region imaged by MLT, the lines $\{l_1, l_2, \ldots, l_i, \ldots, l_8\}$ are oriented parallel to either the vertical or horizontal edges of the cross section segmenting the area into similar squares, and l_s represents the side length of the equivalent-area cross section calculated as $\sqrt{A}$. The width of a dry structural unit is given as:

$$w_{ds} = \frac{l_s}{N_s} \tag{4}$$

where N_s is the number of squares encountered along a transect between 2 parallel sides of the square equivalent-area cross section. In Equation 4, the thickness of the pores, which are represented as labeled dividing line segments in Figure 2, is not accounted for since the cross section explicitly represents the non-macroporous equivalent area. Not counting the edge of the cross section shown in Figure 2, the number of squares is given by:

$$N_s = N_l \tag{5}$$

where N_l is the number of l_i lines dividing the region into squares between two parallel sides of the square equivalent-area cross section (e.g., four in the case of Figure 2). Equation 5 assumes that the imaged cross section does not have macropores that occur at and in parallel with the boundaries of the cross section. The value for N_l can be found as:

$$N_l = \frac{l_T}{2l_s} \tag{6}$$

since half the total length of the dividing line segments (i.e., $l_T = \sum l_i$) are horizontal and the other half are vertical. In other words, $2N_l l_s$ is the total length of the dividing line segments. In the MLT image, the surface scan

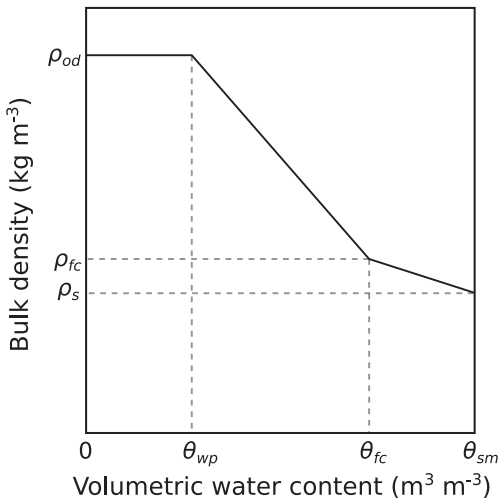

Figure 3. Conceptual plot illustrating the linear interpolation between oven-dried (*od*), field-capacity (*fc*), and saturated (*s*) bulk densities of the matrix (ρ) for the matrix-saturated (*sm*), field-capacity, wilting-point (*wp*) and zero water content (θ) states.

gaps (SSGs) used as a proxy for macropores (Eck et al., 2013) are generally represented as thin areas. Thus, since their perimeters represent both sides of the SSG, the total length l_T can be approximated as half of the total measured SSG perimeter (P) in the MLT image. Finally, w_{ds} can be expressed as:

$$w_{ds} = \frac{2l_s\sqrt{A}}{l_T} \tag{7}$$

which simplifies to:

$$w_{ds} = \frac{4A}{P} \tag{8}$$

Equation 8 is identical to the calculation for average unit size from an MLT image given by Eck et al. (2013).

To predict changes in the w term of Equation 1 as structural units respond to changes in the matrix volumetric water content (θ_m), we derive an expression for $w(\theta_m)$ by linearly interpolating the matrix-saturated bulk density (ρ_s), the commonly measured field-capacity (i.e., the water content in equilibrium with −33 kPa of pressure) bulk density $\left(\rho_{fc}\right)$, and the oven-dried bulk density (ρ_{od}) all expressed on a dry soil basis (Figure 3). From this interpolation, an expression for bulk density (ρ) at time t corresponding to θ_m is given as:

$$\rho(\theta_m) = \begin{cases} \rho_{fc} & : \quad \theta_m \geq \theta_{fc},\ \rho_{fc} \leq \rho_s \\ \theta_m\left(\dfrac{\rho_s - \rho_{fc}}{\theta_{sm} - \theta_{fc}}\right) - \theta_{fc}\left(\dfrac{\rho_s - \rho_{fc}}{\theta_{sm} - \theta_{fc}}\right) + \rho_{fc} & : \quad \theta_m \geq \theta_{fc},\ \rho_{fc} > \rho_s \\ \theta_m\left(\dfrac{\rho_{fc} - \rho_{od}}{\theta_{fc} - \theta_{wp}}\right) + \dfrac{\rho_{od} - \rho_{fc}}{\dfrac{\theta_{fc}}{\theta_{wp}} - 1} + \rho_{od} & : \quad \theta_{wp} < \theta_m < \theta_{fc} \\ \rho_{od} & : \quad \theta_m \leq \theta_{wp} \end{cases} \tag{9}$$

where θ_{fc} is the volumetric field-capacity water content, θ_{wp} is the volumetric wilting-point water content (i.e., the water content in equilibrium with −1500 kPa of pressure), and ρ_s is determined from the matrix-saturated water content (θ_{sm}) as:

$$\rho_s = \rho_p(1 - \theta_{sm}) \tag{10}$$

where ρ_p is the particle density (assumed to be 2,650 kg m^{-3}). Here, ρ corresponds to the bulk density of the structural units. Equation 9 assumes negligible volume change below the wilting point water content. The amount of swelling of a structural unit represented by ρ is given by the coefficient of linear extensibility (*COLE*):

$$COLE(\theta_m) = \left(\frac{\rho_{od}}{\rho(\theta_m)}\right)^{\frac{1}{3}} - 1 \tag{11}$$

The *COLE* in Equation 11 is changed slightly from its normal use as a static metric of maximum swelling potential to a dynamic term dependent on soil water content. Because COLE represents the potential for one-dimensional extension, *COLE* can also be represented as:

$$COLE = \frac{\hat{w}(\theta_m) - w_{ds}}{w_{ds}} \tag{12}$$

which can be rearranged to:

$$\hat{w}(\theta_m) = w_{ds}[1 + COLE(\theta_m)] \tag{13}$$

where $\hat{w}$ is the *COLE*-predicted structural unit width. To obtain the $w(\theta_m)$ represented in Figure 1, we define a correction factor (δ) by which to scale the rate at which the structural unit width changes as a function of θ_m, to prevent the w from exceeding the space available into which it can expand as:

$$\delta = \begin{cases} \dfrac{d_{ds}}{w_{ds}[1 + COLE(\theta_m = \theta_{sm})] - w_{ds}} & : \quad \hat{w}(\theta_m = \theta_s) > W \\ 1 & : \quad \hat{w}(\theta_m = \theta_s) \leq W \end{cases} \tag{14}$$

where $W = w_{ds} + d_{ds}$. The structural unit width can then be defined as:

$$w(\theta_m) = w_{ds}[1 + \delta COLE(\theta_m)] \tag{15}$$

Finally, an expression for macropore width at any matrix water content, θ_m, is given as:

$$d(\theta_m) = W - w(\theta_m) \tag{16}$$

Although it is more common to relate the change in soil volume to change in water content using the volume of the solids to normalize the pore volume (i.e., void ratio) and volume of the water (i.e., moisture ratio) (e.g., Bronswijk, 1988a; Hillel, 1998; Peng & Horn, 2005), we chose to relate these through the bulk density and volumetric water contents as shown in Figure 3 to express this model in terms of readily available variables in large data sets. It is relatively rare to find void ratio and moisture ratio directly in soil databases, whereas bulk density as well as field capacity and wilting point water contents are more common (e.g., National Cooperative Soil Survey, 2025) and can more readily be incorporated into this model. We note that the approach we adopt and domains approximated by the line segments in Figure 3 retain similar meaning to the more traditional soil shrinkage curve (Peng & Horn, 2005) where the change from ρ_s to ρ_{fc} approximates structural shrinkage, the change from ρ_{fc} to ρ_{od} corresponds to a combination of normal and residual shrinkage, and the lack of change in $\rho(\theta_m)$ for water contents less than θ_{wp} corresponds to zero shrinkage.

2.2. Hydraulic Conductivity

Laminar volumetric flow (Q) through a vertical planar slit-shaped macropore under a unit gravitational pressure gradient can be described following Bird et al. (1960) and Lepore et al. (2009) as:

$$Q = \frac{d^3 w \rho_w g}{12\eta} \tag{17}$$

where ρ_w is the density of water in units of kg m^{-3}, g is the acceleration due to gravity, η is the dynamic viscosity of water, and d and w are as previously defined. By rearranging Equation 2 to obtain an expression for w in terms of d, Equation 17 can be rewritten as:

$$Q = \frac{d^3 (W - d) \rho_w g}{12\eta} \tag{18}$$

Because each structural unit is assumed to be a cube, the number of slit-shaped macropores per ground area (D) is given as:

$$D = 2W^{-2} \tag{19}$$

where D is in units of count m^{-2}. Equation 19 follows the derivation of Lepore et al. (2009) where, because each structural unit shares a macropore with a neighboring structuring unit, each cube representing a structural unit will be associated with 6 half slit-shaped macropores (equivalent to 3 full macropores). However, only 2 of those macropores intersect a cross section oriented perpendicular to flow and are counted in Equation 19.

We derive the following expression for saturated hydraulic conductivity of the macropores (K_{sp}) by (a) multiplying Equations 18 and 19 to calculate the flux density, (b) multiplying the gravitational constant by 2/3 to account for the fact that only 2 of the 3 macropores that contribute to viscous drag also contribute to the pressure head (Lepore et al., 2009), and (c) realizing that the flow in Equation 18 is under a unit pressure gradient:

$$K_{sp} = \frac{d^3(W-d)\rho_w g}{9\eta W^2} \tag{20}$$

The saturated hydraulic conductivity of the whole soil (K_s) can then be found using an approach similar to Amer et al. (2009) and Drager et al. (2016):

$$K_s = \left(1 - f_p\right) K_{sm} + f_p K_{sp} \tag{21}$$

where K_{sm} is the saturated hydraulic conductivity of the matrix and f_p is the volumetric fraction of macropores in the whole soil calculated from the total areal fraction of macropores in the MLT image as:

$$f_p = R_p \frac{A_p}{A_{xs}} \tag{22}$$

with the constraint that $0 \leq f_p \leq f_p(\theta_m = \theta_{wp})$. In Equation 22, R_p is a conversion factor calculated as:

$$R_p = \frac{(w+d)^3 - w^3}{(w+d)d(2w+d)} \tag{23}$$

representing the ratio of the volumetric fraction of macropores to the areal fraction of macropores in the cross section (Appendix B). As seen in Equation 23, this ratio is modified as the width of macropores and structural units change, both of which are a function of water content.

Here we note that Equation 21 can be used to calculate the saturated hydraulic conductivity associated with any soil moisture state. That is, where the soil matrix is non-rigid, both f_p and K_{sp} will increase as the matrix water content becomes more unsaturated causing an increase in the K_s describing the soil material at that water content. Although the matrix porosity will decrease as the soil dries due to shrinkage of the structural units thus reducing K_{sm}, in this model, K_{sm} does not directly reduce with decreasing θ_m. Instead, its contribution to K_s is reduced in proportion to the θ_m-induced changes to macroporosity (Equation 21). Adopting the terminology of Stewart, Abou Najm, et al. (2016), we consider K_s in Equation 21 to be a transient saturated hydraulic conductivity that is a function of matrix water content.

A description of the unsaturated hydraulic conductivity (K) function can be derived by coupling the capillary bundle model of Mualem (1976) with the dual porosity water retention function of Durner (1994) to yield (Radcliffe & Šimůnek, 2010):

$$K(S_e) = K_s \frac{\left(w_1 S_{e_1} + w_2 S_{e_2}\right)^l \left\{ w_1 \alpha_1 \left[1 - \left(1 - S_{e_1}^{\frac{1}{m_1}}\right)^{m_1}\right] + w_2 \alpha_2 \left[1 - \left(1 - S_{e_2}^{\frac{1}{m_2}}\right)^{m_2}\right]\right\}^2}{\left(w_1 \alpha_1 + w_2 \alpha_2\right)^2} \tag{24}$$

where S_e is effective soil water saturation given as $\frac{\theta - \theta_r}{\theta_s - \theta_r}$, l is a pore connectivity parameter (commonly assumed to be equal to 0.5), m and n are fitting parameters in the water retention function and often assumed to be related by the equation $m = 1 - \frac{1}{n}$, α is the inverse of the air-entry potential, θ_s is saturated volumetric water content of the soil, and θ_r is residual volumetric water content. The w_1 and w_2 are weighting factors for the matrix and structural

porosity domains, respectively, in the dual porosity water retention function with the subscripts on the S_{e_1}, S_{e_2}, α_1, α_2, m_1, m_2, n_1, and n_2 also corresponding to these two domains. For the matrix domain, the effective saturation is given as:

$$S_{e_1} = \frac{\theta_m - \theta_r}{\phi_m - \theta_r} \tag{25}$$

and for the structural domain:

$$S_{e_2} = \frac{\theta_p}{f_p} \tag{26}$$

with the following constraints:

$$\theta_s = \phi = \phi_m + f_p \tag{27}$$

$$\theta = \theta_m + \theta_p \tag{28}$$

where ϕ_m is the porosity of the matrix (i.e., volume of matrix pores to total soil volume), θ_p is the volumetric macropore water content, and ϕ is total porosity calculated from the bulk and particle densities as:

$$\phi_m(\theta_m) = 1 - \frac{\rho(\theta_m)}{\rho_p} \tag{29}$$

The weighting factor for the matrix domain is calculated using the matrix porosity:

$$w_1(\theta_m) = \frac{\phi_m(\theta_m)}{\phi(\theta_m)} \tag{30}$$

Similarly, the weighting factor for the structural domain is:

$$w_2(\theta_m) = \frac{f_p(\theta_m)}{\phi(\theta_m)} \tag{31}$$

where w_1 and w_2 represent that portion of ϕ that is either matrix pores or structural macropores, respectively. Equations 29–31 make explicit that the total porosity, matrix porosity, and weighting factors are functions of the matrix water content through its effects on bulk density, total porosity, and macropore fraction.

Because the macropore width distribution changes as the structural units shrink and swell in response to changes in matrix water content, the parameters, α_2 and n_2, can be written in terms of θ_m. These parameters can first be fit to MLT-derived data on macropores scanned at a dry state by applying the van Genuchten (1980) water retention function. Considering only the structural domain, this model can be expressed as:

$$\theta_p = \frac{f_p}{[1 + (-\alpha_2 h)^{n_2}]^{1-\frac{1}{n_2}}} \tag{32}$$

where h is matric potential calculated for planar pores in head units as (Dexter, 2004):

$$h = -\frac{\sigma}{\rho_w g d} \tag{33}$$

σ is water surface tension, and ρ_w is water density. Using Equation 33, each macropore width in the MLT-derived image can be converted to a matric potential. The macropore water content corresponding to the ith value of h can be found by computing the cumulative sum of the area of each macropore with widths smaller than or equal to d_i

and dividing by A_{xs}. Equation 32 can be fit to the resulting pairs of θ_{p_i} and h_i values to estimate α_2 and n_2. Because these paramters are estimated from macropores scanned at a dry state, we refer to them as α_{ds} and n_{ds}, respectively.

To estimate α_2 at a wet state, the fractional area and width of each macropore can be adjusted by its width and converted to a volumetric fraction as follows. First, the fractional area of each macropore is multiplied by the ratio of $\frac{d}{d_{ds}}$ to account for the reduction in macropore area in response to an increase in θ_m and corresponding swelling of the matrix. Second, d is used to find the average structural unit width by rearranging Equation 2 and substituting $w_{ds} + d_{ds}$ with W:

$$w(\theta_m) = W - d(\theta_m) \tag{34}$$

The structural unit width is used to define R_p for each θ_m-adjusted macropore width $[d_i(\theta_m)]$ as:

$$R_{p_i}(\theta_m) = \frac{[w(\theta_m) + d_i(\theta_m)]^3 - w(\theta_m)^3}{[w(\theta_m) + d_i(\theta_m)]\, d_i(\theta_m)\, [2w(\theta_m) + d_i(\theta_m)]} \tag{35}$$

and the volume fraction of macropores for each width $\left(f_{p_i}\right)$ is then found as:

$$f_{p_i} = R_{p_i}(\theta_m)\, \frac{A_{p_i} d(\theta_m)}{A_{xs} d_{ds}} \tag{36}$$

where A_{p_i} is the area of the ith macropore in the MLT-scanned cross section (Appendix B). Equation 33 and the cumulative sum of f_{p_i} are used to calculate the corresponding h_i and θ_{p_i} values, respectively. Equation 32 is then fit to the resulting pairs of θ_m-adjusted θ_{p_i} and h_i and the parameters α_2 and n_2 are determined.

A function of the form:

$$\alpha_2(\theta_m) = \alpha_{ds}\beta_0 - \alpha_{ds}\beta_1 \frac{d(\theta_m)}{d_{ds}} \tag{37}$$

can be fit to estimates of α_2 for different values of $\frac{d}{d_{ds}}$ to obtain α_2 for any θ_m where β_0 and β_1 are empirically determined fitting parameters. As discussed below, estimates of n_2 from fits of Equation 32 to the adjusted θ_{p_i} and h_i pairs are insensitive to changes in $\frac{d}{d_{ds}}$ and, thus, θ_m. The value for n_2 is, therefore, assumed to be equal to n_{ds} across the range of θ_m.

Combining the expressions above, Equation 24 can be written as:

$$\begin{aligned} K(\theta, \theta_m) = \; & K_s(\theta_m) \cdot [w_1(\theta_m) S_{e_1}(\theta_m) + w_2(\theta_m) S_{e_2}(\theta - \theta_m, \theta_m)]^l \cdot \\ & \left\{ w_1(\theta_m)\alpha_1 \left[1 - \left(1 - S_{e_1}(\theta_m)^{\frac{n_1}{n_1 - 1}} \right)^{1 - \frac{1}{n_1}} \right] + \right. \\ & \left. w_2(\theta_m)\alpha_2(\theta_m) \left[1 - \left(1 - S_{e_2}(\theta - \theta_m, \theta_m)^{\frac{n_2}{n_2 - 1}} \right)^{1 - \frac{1}{n_2}} \right] \right\}^2 \cdot \\ & (w_1(\theta_m)\alpha_1 + w_2(\theta_m)\alpha_2(\theta_m))^{-2} \end{aligned} \tag{38}$$

Equation 38 makes explicit that there are two water contents inherent in this expression of K. The first is the total volumetric water content of the soil and the second is the volumetric water content of the soil matrix. In this formulation, K_s is a function of θ_m since only water diffused into the matrix would cause the swelling of the structural units depicted in Figure 1 changing the relative volumetric proportions of macropores and matrix as expressed in Equation 21. The θ in the effective soil water saturation term of the structural domain corresponds to a theoretical water content for which K could be calculated assuming that the pore-size distribution of the soil was fixed across all water contents to its state in equilibrium with θ_m. Thus, the unsaturated hydraulic conductivity

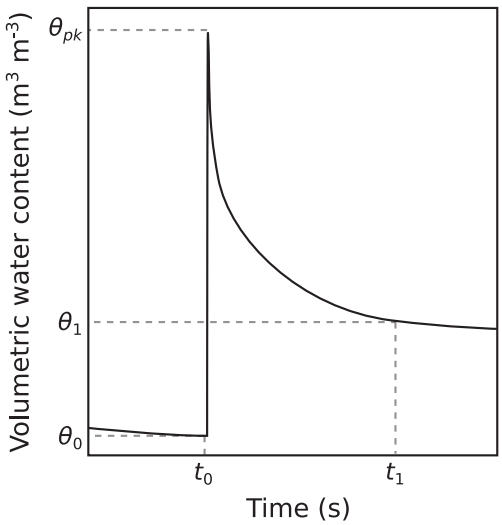

Figure 4. Hypothetical time series of total soil volumetric water content during a preferential flow event representing the downward flux of macropore water occurring just after time t_0. Axes show the relative placement of the antecedent (θ_0) and final matrix water content (θ_1) and their corresponding times (t_0 and t_1) along with the peak total water content (θ_{pk}).

represented in Equation 38 can be thought of as a family of theoretical curves each corresponding to different K_s values determined by θ_m. This would allow K to be visualized as a surface corresponding to a function of θ and θ_m rather than a single curve. The consequences of conceptualizing the unsaturated hydraulic conductivity function as a $K(\theta, \theta_m)$-surface are discussed in Section 4.6. However, we note that from Equations 26 and 28, S_{e_2} can be written as a function of θ_p and θ_m and, therefore, the unsaturated hydraulic conductivity function represented in Equation 38 can alternatively be expressed explicitly as a function of matrix and macropore water contents or their respective degrees of saturation.

2.3. Matrix and Macropore Water Content

The total soil volumetric water content at time t can be partitioned into θ_m and θ_p from an estimate of the rate at which water in macropores is absorbed by the surrounding soil matrix. This approach is similar to event-based recession analysis of hydrographs commonly used to characterize recession behavior of aquifers and estimate storage-discharge functions (Brutsaert & Nieber, 1977; Dralle et al., 2017; Kirchner, 2009). Figure 4 illustrates the total soil water content response to an idealized preferential flow event where water is conducted via macropores to the soil depth and, concurrently, is partially absorbed by the matrix. The discrete time derivative of θ_m is calculated as:

$$\frac{\mathrm{d}\theta_m}{\mathrm{d}t} = \frac{\theta_1 - \theta_0}{t_1 - t_0} \tag{39}$$

where θ_0 and θ_1 are the antecedent and final matrix water contents, respectively, and t_0 and t_1 their corresponding times. The amount of water added during the preferential flow event ($\Delta\theta$) is given as:

$$\Delta\theta = \theta_{pk} - \theta_0 \tag{40}$$

where θ_{pk} is the peak total water content. If multiple events are identified in a time series of θ, a corresponding set of $\frac{\mathrm{d}\theta_{m_i}}{\mathrm{d}t}$, $\Delta\theta_i$, and θ_{0_i} values can be determined and fit with the following power law function:

$$\frac{\mathrm{d}\theta_m}{\mathrm{d}t} = \gamma_0 \Delta\theta^{\gamma_1} \theta_0^{\gamma_2} \tag{41}$$

where γ_0, γ_1, and γ_2 are empirically determined coefficients of the model. Equation 41 relates the rate of change in θ_m due to absorption of water from the macropores to the amount of water added to that depth ($\Delta\theta$) as well as the antecedent matrix water content. This is because the potential energy gradient driving the absorption of water into the soil matrix is assumed to be a function of the amount of water added to the macropores (i.e., $\Delta\theta$) as well as the initial matric potential of the soil matrix determined by θ_0. Finally, θ_m at time t_i can be determined from θ as:

$$\theta_m(t_i) = \theta_m(t_{i-1}) + \Delta t \gamma_0 [\theta(t_i) - \theta_m(t_{i-1})]^{\gamma_1} [\theta_m(t_{i-1})]^{\gamma_2} \tag{42}$$

and θ_p determined as:

$$\theta_p(t_i) = \theta(t_i) - \theta_m(t_i) \tag{43}$$

where Δt is the time step between contiguous observations of θ calculated as $t_i - t_{i-1}$.

3. Materials and Methods

3.1. Site Description

To apply the theoretical constructs developed above to relevant in situ data, we conducted a study at the Konza Prairie Biological Research Station (KPBS) approximately 5 km south of Manhattan, Kansas, in a cultivated field as part of a larger project examining soil-climate-land use interactions. A representative agricultural pit (hereafter the Konza APT soil) was opened and described by the US Department of Agriculture–Natural Resources Conservation Service (USDA-NRCS) to a depth of 2 m (N 39.10401°W 96.60728°; Pedon ID: S2018KS161104) and classified as a fine-silty, mixed, superactive, mesic Pachic Vertic Argiudoll. The pedon is located within a tread of a lowland flood plain terrace mapped as the Reading series with a slope of approximately 1%. We chose the Reading series for this investigation since it is known to display morphological evidence of shrink-swell behavior (e.g., presence of slickensides) and has a subsurface clay mineralogy influenced by montmorillonite; we expected this soil to display characteristics of dynamic porosity that would be important for soil hydraulic properties. Mean annual temperature for the KPBS is 12.8°C and mean annual precipitation is between 835 and 851 mm with approximately 70%–75% of this precipitation falling during the growing season between May and September (Caplan et al., 2019; Slette et al., 2022).

3.2. Soil Sampling and Sensor Installation

Bulk samples and clods were taken by the USDA-NRCS from each morphological horizon for physical and chemical analysis. Three intact soil monoliths were collected in steel trays (30 cm wide × 40 cm deep × 4 cm thick) corresponding to the morphological horizons—Ap1 (0–15 cm), Bt (26–47 cm), and Btkss2 (113–139 cm)—in which soil water content sensors would be later installed as part of a separate study. Monoliths were excavated by pressing the tray onto the vertical soil profile wall and marking its location with a trowel. Trays were then set aside and the marked location of each side of the tray on the soil profile wall was used to carve an approximately 4-cm outside perimeter into the soil pit face using hand tools. This perimeter was carved until a tray-shaped soil block was left in relief. Trays were then fitted around this block and slowly pressed toward the profile wall until the tray was filled with the soil monolith. The soil was then perforated using soil knives from the sides and top of the tray to separate it from the profile wall. Monoliths were immediately laid flat to avoid soil loss and subsequently carved and leveled so that only approximately 1 cm of the soil remained above the sides of the tray. Monoliths were then wrapped with saran and bubble wrap, transported with care back to the laboratory to avoid damaging the soil structure, and stored in a cold, dark room at ∼4°C until analysis.

While the pit was open, soil moisture and temperature sensors (ECH2O 5TM, METER Group, Pullman, WA) were installed into the soil profile wall at a depth of 10, 40, and 120 cm and connected to a data logger (CR1000X, Campbell Scientific, Logan, UT). Soil moisture and temperature sensors were set to collect data every 30 min between 26 October 2018 and 24 January 2020. No data were collected from any of the sensor depths between 17 May 2019 and 12 June 2019 due to a malfunction with the data logger.

3.3. Multistripe Laser Triangulation Scanning

Soil monoliths were prepared for MLT scanning in the laboratory by carving the soil until it was flat and level just above the edge of the steel tray. The surface was then treated with 1,1-difluoroethane following Hirmas (2013) to flash freeze an approximately 10 × 10 cm thin layer of the monolith at a time and peeled to remove artifacts left behind during the carving process. To facilitate the detection of macropores by MLT, trays were brought to a dry-state by oven drying at 60°C for 24 hr to induce maximum shrinkage of the structural units and exaggerate macropore size. Monoliths were then scanned with an MLT scanner (3D Scanner Ultra HD, NextEngine, Inc., Santa Monica, CA) in a dark room. Approximately 20 scans per tray were taken in macro mode (i.e., 100 μm point spacing) to get complete coverage of the monolith. Scanned areas represented overlapping regions on the surface of the monolith and were stitched together using ScanStudio (NextEngine, Inc., Santa Monica, CA). Details of the scanning and stitching process are provided by Eck et al. (2013).

Scans were transferred to RapidWorks (NextEngine, Inc., Santa Monica, CA) and outputted as space-delimited text files (.asc) containing 9 columns: the x, y, and z coordinates of the point cloud, R, G, and B color values for each point, and the 3 indices of the unit vector indicating the facing direction of the facet associated with each point. Files were read into R (R Core Team, 2024) and converted to black and white. tiff files by recording the

presence (white) or absence (black) of points on a 180-μm grid overlain on the point cloud data from each monolith. The resulting MLT-derived image was read into ImageJ (Schneider et al., 2012), cropped to the appropriate horizon depths, and the geometric properties of the SSGs represented by the absence of points on the projected plane (i.e., black regions) were analyzed following Eck et al. (2013) and recorded in a comma-delimited file (.csv). Geometric properties included the perimeter, area, and minimum Feret diameter (i.e., minimum caliper distance) of each pore and the total area of the image. The output file containing the properties of each SSG were then read back into R and only gaps with areas larger than π mm^2 corresponding to equivalent circular radii of 1 mm were considered macropores and used in the analysis of macropore properties following Eck et al. (2016). This value corresponds to the projected area of a single very coarse sand grain and provides a convenient threshold to correctly identify macropores in the MLT image. The geometric mean of the minimum Feret diameter was calculated for each horizon from the individual pore data and used as the value of d_{ds}.

3.4. Laboratory Analyses

Samples were analyzed in the USDA-NRCS Kellogg Soil Survey Laboratory for soil physical properties following standard procedures (Soil Survey Staff, 2014). Silt and clay were determined using the pipette method following pretreatment with H_2O_2 to remove soil organic matter and sand was determined gravimetrically after passing samples through a 0.047 mm sieve following dispersion with $(NaPO_3)_6$. Soil clods were analyzed for bulk density after equilibrating the water content of the samples to −33 kPa of soil water potential and again after oven drying. Water content of samples equilibrated to −33 and −1500 kPa of pressure were determined gravimetrically and recorded as the field capacity and wilting point water contents, respectively. These values were converted to a volumetric basis using the field capacity bulk density for θ_{fc} and oven-dried bulk density for θ_{wp}. Values of sand, silt, and clay were used as inputs into the pedotransfer function ROSETTA (Schaap et al., 2001) to estimate θ_{sm}, θ_r, α_1, n_1, and K_{sm} corresponding to the matrix domain in Equation 38 of each horizon.

Soil shrinkage values were measured using a modified *COLE* method (Schafer & Singer, 1976). Saturated pastes from sieved (<2 mm) samples collected from each depth were extruded through a syringe with a 1-cm diameter opening on pre-weighed smooth plastic weigh boats in triplicate to create rods with lengths between 50 and 100 mm. Separate aliquots of each saturated paste were determined for gravimetric water content. Weigh boats and rods were weighed after air-drying at 0, 2, 4, 8, 24, and 48 hr after extrusion and the rod lengths recorded. Gravimetric water content for each measurement time was calculated using the initial water content of the saturated paste and mass of each rod to determine the amount of water loss due to drying over that time period. The rod length at 48 hr corresponded with the final shrinkage length of the rod (r_f). The rod lengths at 0–24 hr were used to calculate *COLE* values as:

$$COLE(u_{m_i}) = C_0 + C_1\left(\frac{r_i(u_{m_i}) - r_f}{r_f}\right) \tag{44}$$

where r_i and u_{m_i} are the rod length and gravimetric water content determined at the ith time step, respectively, and C_0 and C_1 are fitting parameters empirically determined by Schafer and Singer (1976) to be 0.0124 and 0.571, respectively. Bulk density values corresponding to each measured u_m were determined by rearranging Equation 11:

$$\rho(u_{m_i}) = \frac{\rho_{od}}{[COLE(u_{m_i}) + 1]^3} \tag{45}$$

and the bulk density converted to porosity following Equation 29.

3.5. Data Analyses

3.5.1. Partitioning Macropore and Matrix Water Content

Soil water content from sensor data installed at each depth was partitioned into matrix and macropore water content following the procedure illustrated in Figure 5. Briefly, peaks were identified from time derivative water content data estimated with a Savitzky-Golay filter using a second-order polynomial fit to a 24-hr moving window with the savgol function in the *R* package pracma (Borchers, 2023). A Hampel filter was used to calculate the

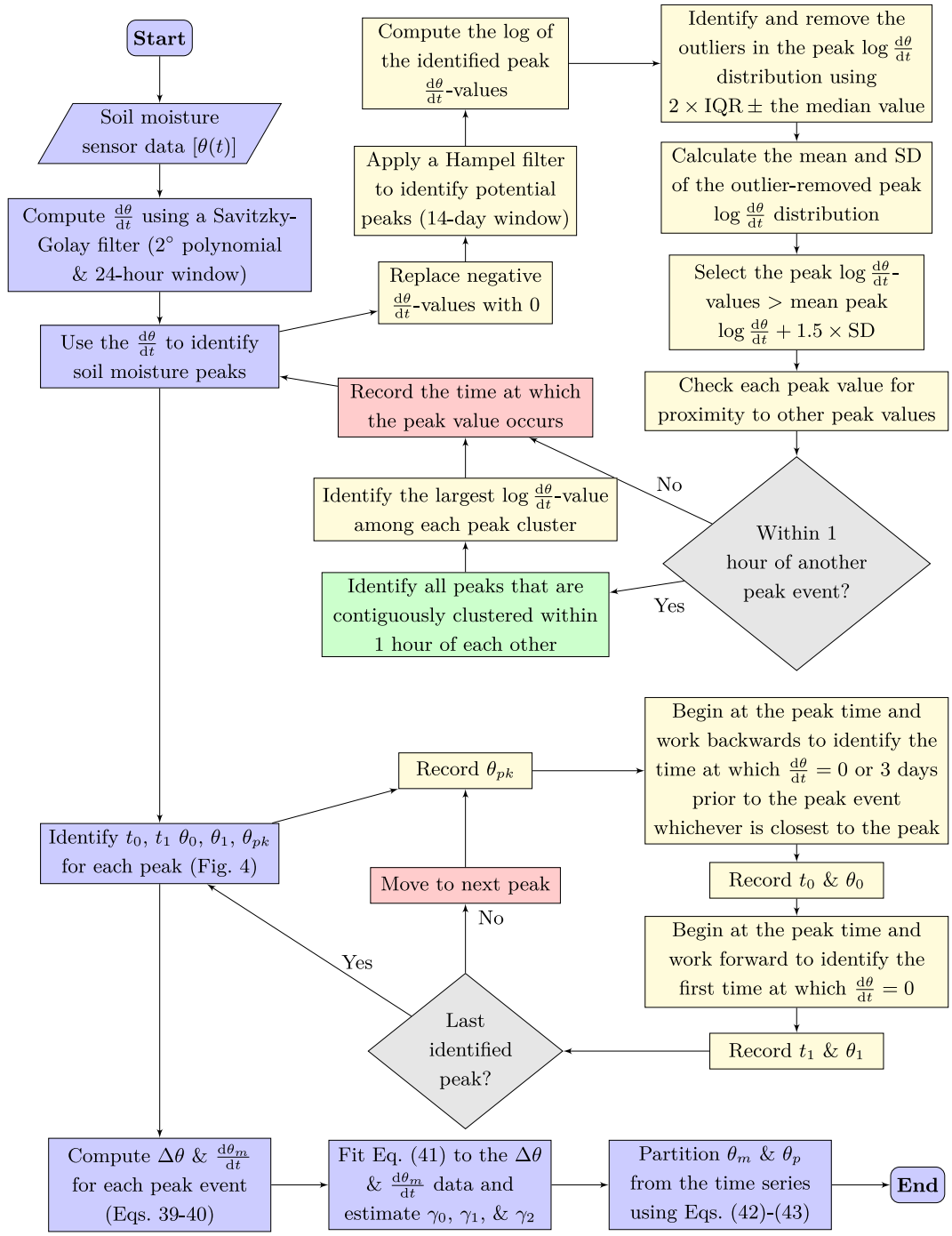

Figure 5. Procedure used in this study for partitioning soil moisture values from sensor data into matrix and macropore water content.

median absolute deviation (MAD) of each derivative value in the time series and values greater than 3 MAD above the median calculated from a 14-day moving window were used to identify potential peaks with the hampel function in the pracma package. Outliers in the Hampel-filter identified peak derivative distribution were categorized as being above or below twice the interquartile range as the median value in log space and removed. The resulting peak log derivative distribution was further filtered to include only those peak values that were greater than 1.5 times the standard deviation of the peak log derivative mean. Finally, peaks were selected that were

separated by at least an hour from each other or that represented the largest derivative value among initially identified clusters of peaks and the corresponding values of θ_{pk} were recorded.

The t_0 and θ_0 corresponding to each peak were identified by finding a time closest to but before the peak event where $\frac{d\theta}{dt} = 0$. If the time derivative did not equal zero within 3 days prior to the peak event, t_0 was set to 3 days before and the θ_0 recorded. Similarly, t_1 and θ_1 were identified as the first time after the peak event when $\frac{d\theta}{dt} = 0$. The $\frac{d\theta_m}{dt}$ and $\Delta\theta$ of each peak were calculated following Equations 39 and 40, respectively, and a linearized Equation 41 was fit to the resulting data in R to estimate the values and standard errors of the parameters γ_0, γ_1, and γ_2. Matrix and macropore water contents were subsequently calculated from Equations 42 and 43. The first measured θ in the time series was assumed to be equivalent to θ_m (i.e., $\theta_p = 0$).

3.5.2. Macropore Water Retention

The area and minimum Feret diameter of each macropore identified in the MLT image were converted to a volume fraction using Equation 36 and the cross-sectional area of the image. A vector of macropore water contents ($\boldsymbol{\theta}_\mathbf{p}$) was calculated as the cumulative sum of ordered volumetric fractions of increasing pore widths as:

$$\boldsymbol{\theta}_\mathbf{p} = \begin{bmatrix} \sum_{i=1}^{1} f_{p_i} \\ \sum_{i=1}^{2} f_{p_i} \\ \vdots \\ \sum_{i=1}^{N} f_{p_i} \end{bmatrix} \tag{46}$$

where N is the total number of macropores identified in the MLT image. Similarly, a vector of matric potentials ($\mathbf{h}$) corresponding to each element in $\boldsymbol{\theta}_\mathbf{p}$ was calculated following Equation 33. Equation 32 was then fit to the water content and matric potential vectors using the nlrob function of the robustbase package (Maechler et al., 2024) in R and the estimates and standard errors determined for the parameters α_2 and n_2. The values of the elements in $\boldsymbol{\theta}_\mathbf{p}$ and $\mathbf{h}$ were then adjusted for 100 θ_m values evenly distributed in the interval $[\theta_{wp}, \theta_{sm}]$ for each horizon in the study, Equation 32 refit to the θ_m-adjusted vectors, and new estimates for the α_2 and n_2 parameters recorded. Equation 37 was fit to values of α_2 in R and the estimates and standard errors for the parameters β_0 and β_1 were recorded. Estimates of α_2 determined from fitted parameters in Equation 37 were plugged into Equation 32 along with the n_2 value determined at a dry-state and $f_p(\theta_m)$ to predict θ_p for any value of θ_m. The Nash-Sutcliffe efficiency (NSE) was calculated for each fit as (Nash & Sutcliffe, 1970):

$$\text{NSE} = 1 - \frac{\sum_{i=1}^{N} \left(\theta_{p_i} - \hat{\theta}_{p_i}\right)^2}{\sum_{i=1}^{N} \left(\theta_{p_i} - \bar{\theta}_p\right)^2} \tag{47}$$

where θ_{p_i} is the calculated θ_m-adjusted water content for macropores widths less than or equal to d_i, $\hat{\theta}_{p_i}$ is the corresponding model (i.e., Equation 32) predicted θ_m-adjusted macropore water content, and $\bar{\theta}_p$ is the mean macropore water content associated with θ_m.

3.5.3. Model Comparison

To assess the validity of dynamic porosity and hydraulic conductivity predictions from this study, soil shrinkage curve measurements were first fit with a model proposed by Stewart, Rupp, et al. (2016) describing the change in structural unit porosity (i.e., referred to as aggregate porosity by those authors and matrix porosity in this study) as a function of normalized gravimetric water content $\left(U = \frac{u_m}{u_{\max}}\right)$ as:

$$\phi_m(U) = \left(\phi_{\max} - \phi_{\min}\right)\left(\frac{p+1}{p+U^{-q}}\right) + \phi_{\min} \tag{48}$$

where $\phi_{\min}$ is the minimum porosity of the matrix, $\phi_{\max}$ is the total porosity of the soil, u_m is gravimetric water content of the matrix, $u_{\max}$ is gravimetric water content of the matrix at saturation, and p and q are fitting parameters that describe the shape of the soil shrinkage curve. Equation 48 was fit to the shrinkage curve data using the nlrob function of the robustbase package (Maechler et al., 2024) in R with all four parameters ($\phi_{\min}$, $\phi_{\max}$, p, and q) free to vary.

We used the fitted variables in Equation 48 to parameterize the following model for transient K_s proposed by Stewart, Abou Najm, et al. (2016):

$$K_s = K_{cmax}\left(\frac{\phi_c(U)}{1-\phi_b(U)}\right)\left(\frac{1-U^q}{1+pU^q}\right)^2 + K_{sm}\left(\frac{1-\phi_{cb}(U)}{1-\phi_b(U)}\right)\left(\frac{p+1}{p+U^{-q}}\right) \tag{49}$$

where K_{cmax} is the saturated (i.e., maximum) hydraulic conductivity of the cracks (macropores) when the matrix is dry (i.e., $U = 0$), ϕ_c is macropore porosity, ϕ_b is subsidence porosity, and ϕ_{cb} is the sum of ϕ_c and ϕ_b. The macropore porosity was determined as:

$$\phi_c = \left\{(\phi_{\max}-\phi_{\min}) - 1 + \left[1-(\phi_{\max}-\phi_{\min})\right]^{\frac{1}{\chi}}\right\}\left(\frac{1-U^q}{1+pU^q}\right) \tag{50}$$

where χ is a shrinkage geometry factor assumed to be equal to 3 in this study corresponding to isotropic shrinkage (Stewart, Abou Najm, et al., 2016). Similarly, ϕ_b was found as:

$$\phi_b = \left\{1-\left[1-(\phi_{\max}-\phi_{\min})\right]^{\frac{1}{\chi}}\right\}\left(\frac{1-U^q}{1+pU^q}\right) \tag{51}$$

and ϕ_{cb} was calculated as:

$$\phi_{cb} = (\phi_{\max}-\phi_{\min})\left(\frac{1-U^q}{1+pU^q}\right) \tag{52}$$

Because K_{cmax} in Equation 49 is treated as a fitting parameter in Stewart, Abou Najm, et al. (2016), we set it equal to the maximum K_{sp} determined from this study following Equation 20 where $d = d_{ds}$. The saturated hydraulic conductivity of the matrix (assumed to be the maximum K_{sm}) was determined with the ROSETTA pedotransfer function (Schaap et al., 2001) using sand, silt, and clay content as inputs. Values of K_s and f_p predicted from this study were then compared to predictions of K_s and ϕ_c computed from the Stewart, Abou Najm, et al. (2016) model, respectively.

4. Results and Discussion

4.1. Response of the Macropore Water Retention Curve to Matrix Water Content

Rescaled macropore width (i.e., $\frac{d}{d_{ds}}$), predicted at various soil matrix water contents for the Ap1 horizon, was directly proportional to the normalized α_2 parameter (i.e., $\frac{\alpha_2}{\alpha_{ds}}$), fit with the van Genuchten (1980) function (Equation 32) to each θ_m-adjusted macropore-size distribution (Figure 6a). The results show a nearly perfect 1:1 correspondence as indicated by the values for the β_0 and β_1 parameters (Equation 37) in Table 1. The Bt and Btkss2 horizons showed a similar result (Table 1) indicating that α_2 can be predicted for any soil matrix water content using the θ_m-modified values of d. These values are higher than commonly attained α values from fits to measured water retention data. This is because the values in Table 1 correspond to macropores with extremely small bubbling pressures due to their large effective diameter; such macropores are not measureable with traditional water retention techniques both because of methodological limitations in this low suction range (Hunt et al., 2013) and, more importantly, because these pores are not fully open under the saturation-state required for their measurement. Interestingly, the values for n_2 were insensitive to refitting Equation 32 for different matrix water contents. Mean n_2 parameter values across the full range of θ_m did not vary from the value of the parameter determined at a dry state (i.e., mean $\frac{n_2}{n_{ds}}$ values were all within 1 standard error of unity; Table 1). Thus, n_2 for the

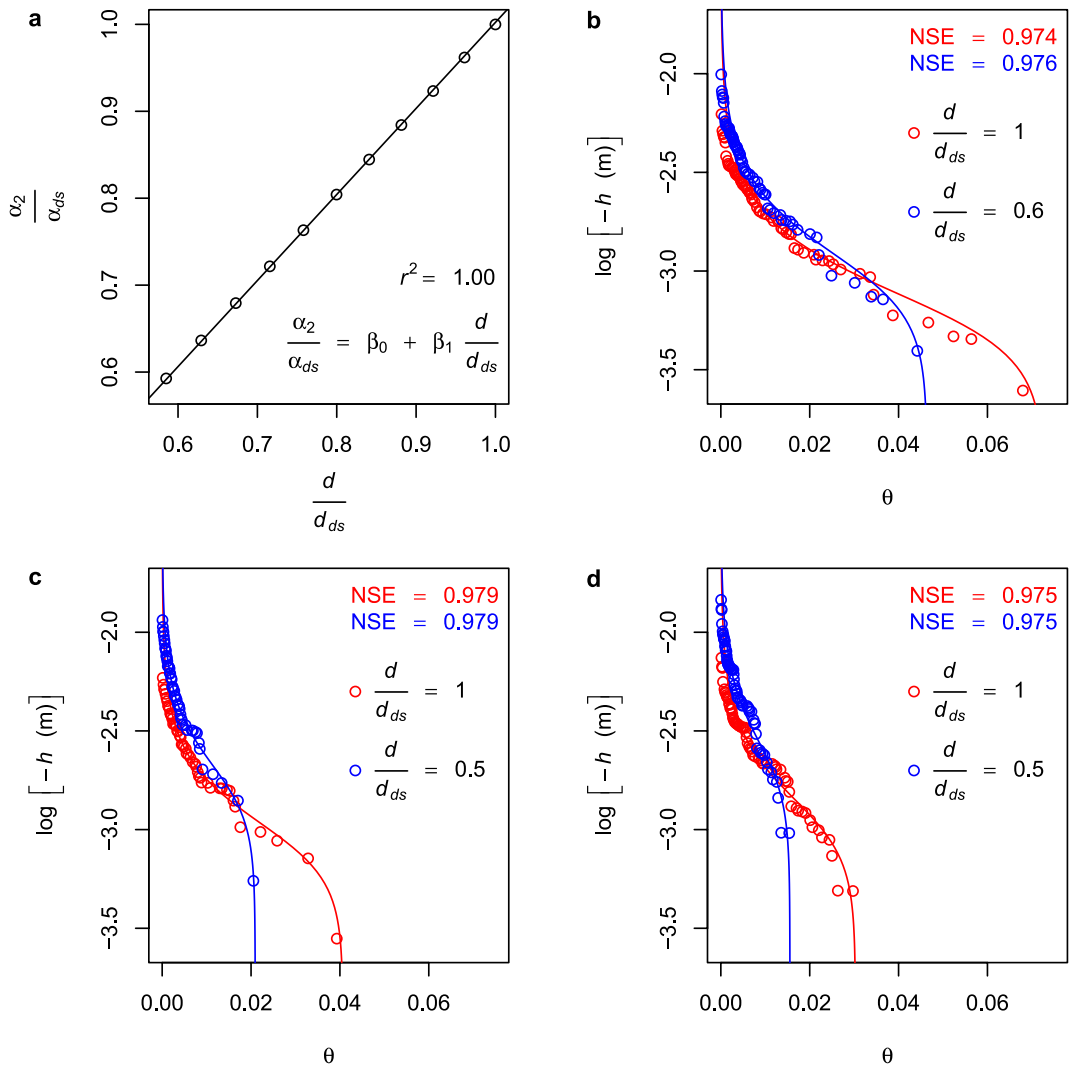

Figure 6. Relationship between α_2 normalized by α_{ds} and different values for the ratio $\frac{d}{d_{ds}}$ with the fitted values for β_0 and β_1 shown in Table 1 for (a) the Ap1 horizon (0–15 cm). Water retention data converted from macropore width determinations for each pore identified in the MLT image scanned at an air-dried state ($d = d_{ds}$) and recalculated for a wetter soil moisture state corresponding to the midpoint of the possible d range shown in red and blue, respectively, for the (b) Ap1, (c) Bt (26–47 cm), and (d) Btkss2 horizons (113–139 cm). Lines shown in (b–d) are calculated from the van Genuchten (1980) function (Equation 32) using the parameters: f_p determined at either the dry or wet state as appropriate, n_2 determined from the fit at the air-dried state, and α_2 determined from the model displayed in panel (a). Nash-Sutcliffe efficiency (NSE) for each model is shown in the upper right hand corner of panels (b–d).

Table 1
Water Retention Curve Parameters, α_2 and n_2, for the Structural Domain Fit Using a van Genuchten (1980) Function to Macropores Determined From MLT-Scanned Monoliths at an Air-Dried State (α_{ds} and n_{ds}), Empirical Parameters (β_0 and β_1) and Residual Standard Errors (RSE) for the Function Represented by Equation 37, and Mean n_{ds}-Normalized n_2 Values

Horizon	Depth (cm)	α_{ds} (m^{-1})	β_0	β_1	RSE	n_{ds}	Mean (n_2/n_{ds})
Ap1	0–15	1,528	0.0124 ± 0.0003	0.990 ± 0.0005	0.0010	2.78	1.000 ± 0.0003
Bt	26–47	1,053	0.0035 ± 0.0003	1.000 ± 0.0005	0.0015	3.06	0.999 ± 0.0005
Btkss2	113–139	807	0.0032 ± 0.0003	1.000 ± 0.0005	0.0013	2.91	0.998 ± 0.0013

Note. Values following ± symbols represent standard errors of the parameters.

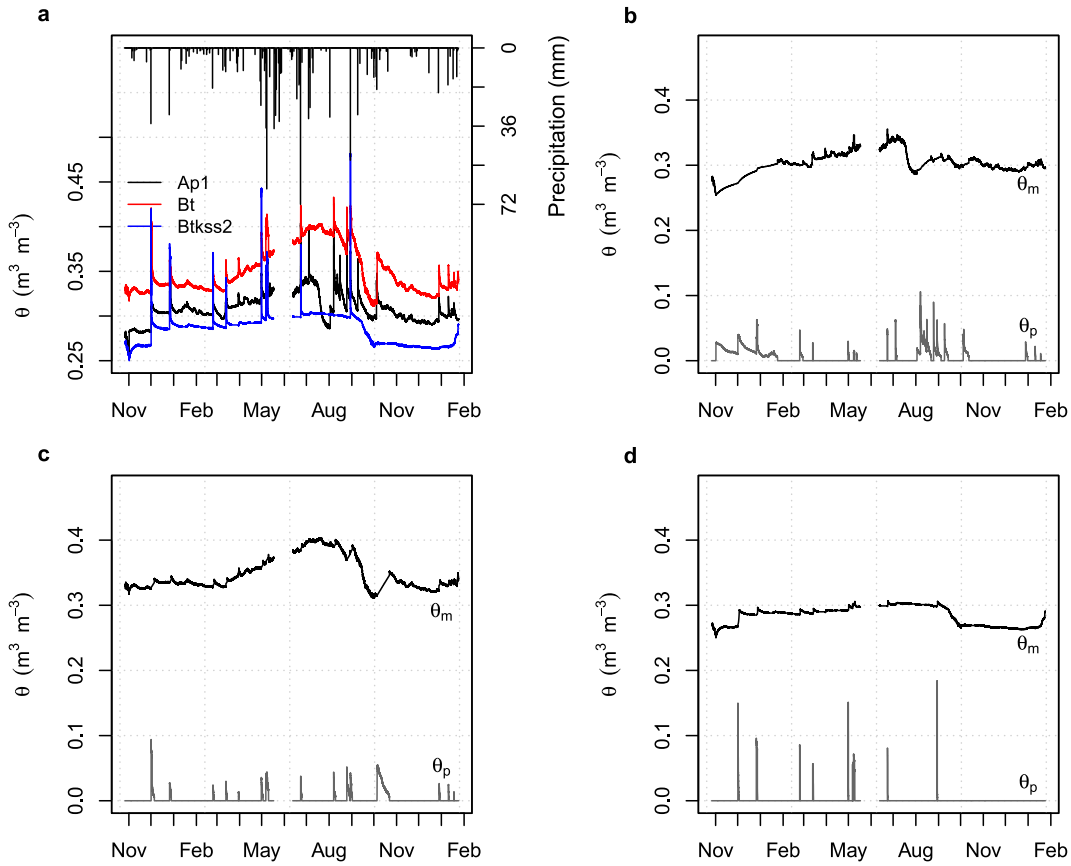

Figure 7. Soil moisture time series data from the Konza APT soil showing (a) total soil water content obtained from three depths corresponding to the indicated soil horizons and calculated matrix (θ_m) and macropore (θ_p) water contents for the (b) Ap1 (0–15 cm), (c) Bt (26–47 cm), and (d) Btkss2 (113–139 cm) horizons. Daily precipitation values at KPBS are shown in panel (a).

macropore domain can be predicted for any matrix water content by estimating it at the dry state under which conditions the MLT scan is obtained.

The results of using Equation 37-predicted values of α_2 from the β_0 and β_1 parameters in Table 1 and n_2 estimated from the fit to macropore-size distribution data at the dry state for each horizon are shown in Figures 6b–6d. The open circles in these panels show water retention data converted from macropore width determined from the MLT-derived image at the air-dried state (shown in red) in which the image was obtained and recalculated for a wetter value (i.e., a water content that corresponded to the midpoint of the possible macropore width range for each respective horizon; shown in blue). Nash-Sutcliffe efficiencies between model-predictions (solid lines in Figure 6) and water retention data for the macropore domain varied little between horizons or matrix water content and showed strong predictive power of the model with values between 0.97 and 0.98. Figures 6b–6d also sheds light on why the shape parameter of the van Genuchten (1980) function used to describe the macropore domain (i.e., n_2) does not change with matrix water content—that is, the fits are scaled to effective saturation of the macropore domain (Equation 26) causing the shape to remain unchanged. The result of modifying macropore width with matrix water content, therefore, is that the curve is shifted up or down resulting in a change in α_2 but not in n_2.

4.2. Macropore and Matrix Water Content

Figure 7a shows daily precipitation at KPBS and soil volumetric water contents for the Ap1, Bt, and Btkss2 horizons of the Konza APT soil during this study. In each horizon, periods of considerably rapid increase in water content corresponding to precipitation events followed by a longer exponentially shaped decline can be observed. Utilizing the procedure outlined in Figure 5, these periods were isolated and fit with a stepwise, linearized form of

Table 2
Fitting Parameters and Diagnostics From the Stepwise Fit of the Power Law Function Represented by Equation 41

Horizon	Depth (cm)	$\ln[\gamma_0\ (s^{-1})]$	γ_1	γ_2	r^2	RSE	P-value $(H_0 : \gamma_1 = \gamma_2 = 0)$
Ap1	0–15	−13.7 ± 1.78	1.27 ± 0.549	—	0.277	1.19	0.036
Bt	26–47	−17.7 ± 0.32	—	—	—	1.10	—
Btkss2	113–139	−44.8 ± 4.88	−1.25 ± 0.341	−18.8 ± 3.81	0.898	0.356	0.01

Equation 41 resulting in the values of the fitting parameters shown in Table 2. Because the stepwise procedure retains variables with the greatest explanatory power, if selected, the values for these fitting parameters can be used to infer potential mechanistic controls on the flux of water through a given horizon. The selection of γ_1, for instance, indicates that the total amount of water added to the horizon controls the transfer of water from the macropore to the matrix, whereas γ_2 indicates that the antecedent water content of the matrix—independent of the amount of water added—is important for this transfer. The $\ln\gamma_0$ in Table 2 represents the intercept in the linearized form of Equation 41.

The stepwise fits indicate that macropore water is most quickly absorbed into the matrix in the Ap1 horizon, more slowly transferred in the Bt horizon, and virtually impeded in the Btkss2 horizon given the increasingly negative $\ln\gamma_0$ values, respectively (Table 2). The amount of water added in a given time step through the macropores was important for predicting the rate at which the water transferred from the macropore to the matrix in the Ap1 horizon, and the positive sign of γ_1 indicates that increased water to the horizon via macropores increases the rate at which the water is absorbed into the matrix. The values and sign of the γ_1 and γ_2 for the Btkss2 horizon indicates the more macropore water added to that horizon in a given time step, the slower the transfer to the matrix (γ_1) and the greater the antecedent water content of the matrix, the greater the difficulty in transferring macropore water to the matrix (γ_2). However, these coefficients should be interpreted with caution since the extremely low γ_0 value (Table 2) largely precludes water absorption into the matrix in the Btkss2 horizon. As represented by the lack of significant γ_1 and γ_2 values in the Bt horizon, the rate at which macropore water is transferred to the matrix is independent of either the amount of macropore water added or the antecedent matrix water content.

These horizon differences are not likely to be predominantly a function of soil texture which was similar across the depths in this profile (Table 3 and see Tables S1 and S2 in Supporting Information S1). Instead, they may be reflective of structural unit packing density (represented by bulk density) and/or soil morphological differences. For instance, the ability of the Ap1 horizon to relatively easily absorb water into the matrix from macropores and the increased rate with greater amounts of macropore water being added, independent of antecedent matrix conditions, is likely due to the comparatively low bulk density (Table 3), friable moist consistence, and moderate thin platy soil structure described in the field. This latter property increases interpedal pore tortuosity that would increase surface area and contact time with the structural units allowing greater rates of absorption into the matrix with greater additions of macropore water. The presence of slickensides indicates both considerable shrink-swell behavior of the Btkss2 horizon and highly compacted and oriented clay skins on the surfaces of structural units. These slickensides along with the high bulk density and very firm moist consistence assessed in the field reflect conditions that would impede the movement of water into the matrix of this horizon from top-down macropore flow. The negative relationship between rate of absorption into the matrix and antecedent matrix water content (i.e., the negative γ_2) in this horizon is likely due to (a) the reduced size of the macropores at high θ_m values which reduces the volume of macropore water available to absorb into the matrix and (b) the larger matric potentials of

Table 3
Selected Soil Properties of the Horizons Used in This Study

Horizon	Depth (cm)	Sand (%)	Silt (%)	Cla (%)	ρ_{fc} (kg m^{-3})	ρ_{od} (kg m^{-3})	θ_{fc} (m^3 m^{-3})	θ_{wp} (m^3 m^{-3})
Ap1	0–15	7.6	53.3	39.1	1,440	1,620	0.307	0.212
Bt	26–47	4.7	52.5	42.8	1,460	1,770	0.380	0.244
Btkss2	113–139	8.1	51.5	40.4	1,560	1,800	0.356	0.254

Note. Sand, silt, and clay content were used as input parameters into the pedotransfer function ROSETTA (Schaap et al., 2001) to predict hydraulic properties for the matrix (see Table 4).

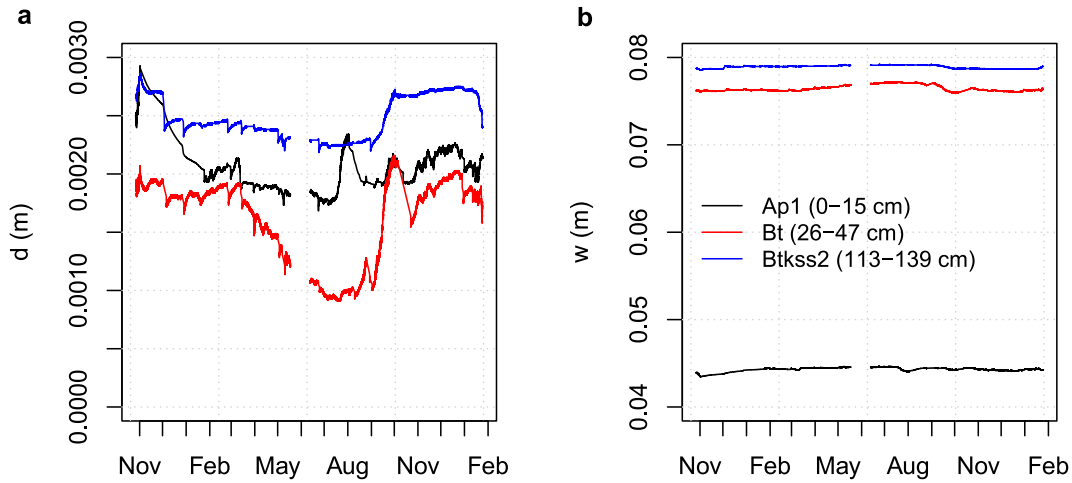

Figure 8. Results of the theory applied to the soil moisture time series for the Ap1, Bt, and Btkss2 horizons in the Konza APT soil showing (a) mean macropore width and (b) mean structural unit width. Time series shows data between 26 October 2018 and 24 January 2020.

the structural units (i.e., less negative) at greater matrix water contents reducing the potential energy gradient responsible for the transfer of water between the macropore and the matrix. In addition, we note that prominent, irregular, cemented, <2 mm-diameter masses of carbonate were observed throughout this horizon which may have reduced the available matrix pore volume leading to less absorption at higher antecedent water content states. Taken together, these findings and the approach of fitting Equation 41 to data derived from soil moisture time series are likely to have significant implications for modeling soil water flow and the transport of clay and SOC at depth in addition to providing a means by which soil morphological information can be integrated into soil moisture sensor data to infer mechanisms relevant to soil hydrology.

We applied Equations 42 and 43 to the time series water content data for each horizon using the respective coefficients in Table 2. The results of this partitioning of θ into θ_m and θ_p are shown in Figures 7b–7d. Here we note that the markedly peaked distribution of macropore water content in the Btkss2 horizon compared to the greater residence time of macropore water in the Ap1 and Bt horizons corresponds with the low matrix absorption fitting parameters and morphological properties described above. Using the partitioned matrix water content values in Figures 7b–7d, we calculated mean macropore and structural unit widths for each horizon using Equations 15 and 16 (Figure 8).

4.3. Response of Structural Unit and Macropore Width to Matrix Water Content

The two panels in Figure 8 present an interesting contrast. The model predicts that while structural unit size changes little relative to its average over the course of the year (Figure 8b), macropore widths change significantly (Figure 8a). The largest average macropore width was observed for the Btkss2 horizon followed by the Ap1 and Bt horizons. This finding is consistent with the interpretations of the matrix absorption fitting parameters (especially γ_2) for this horizon where larger macropores would increase the flux of water through these pores and reduce matrix absorption rates. Macropore width responded to precipitation-induced changes in matrix water content with a noticeable seasonal decrease for the Bt1 horizon between March and July 2019 corresponding to observed increases in soil water content (see Figure 7) followed by a subsequent increase until October 2019. For the Ap1 horizon, average macropore width generally fluctuated around 2 mm with an increase observed just after the installation of the sensors corresponding to the lowest θ_m values. The Btkss2 horizon showed the lowest values between December 2018 and October 2019 corresponding to the highest observed water contents in the matrix over the period of study in this horizon.

As noted above, the smallest macropore width averaged across the study period was found in the Bt horizon with the Ap1 and Btkss2 horizons having consistently larger values. This appears to correspond with the structural grades recorded in the field for these horizons with the Bt horizon described as having weak and moderate grades compared to the Ap1 and Btkss2 horizons both described as moderate. Since structural grade describes the

Table 4
Hydraulic Properties of the Matrix Predicted From ROSETTA (Schaap et al., 2001) and Soil Macroporosity Properties Determined From the MLT-Derived Image of Each Horizon in This Study

Horizon	Depth (cm)	θ_r (m^3 m^{-3})	θ_{sm} (m^3 m^{-3})	α_1 (m^{-1})	n_1	$\log[K_{sm}$ (m s^{-1})]	A_{xs} (m^2)	A_p (m^2)	P (m)	d_{ds} (m)
Ap1	0–15	0.0971	0.4920	1.06	1.44	−5.829	0.0386	0.001945	3.43	0.00365
Bt	26–47	0.1012	0.5032	1.20	1.41	−5.814	0.0360	0.000995	1.86	0.00306
Btkss2	113–139	0.0979	0.4933	1.11	1.43	−5.815	0.0494	0.001014	2.46	0.00286

distinctness of individual structural units (Soil Science Division Staff, 2017), the slightly lower grade of the Bt horizon may correspond to narrower interpedal pores that reduced the apparent expression of soil structure in this horizon.

4.4. Comparing Predictions of Transient Saturated Hydraulic Conductivity Against a Multidomain Dual-Permeability Model

The van Genuchten (1980) water retention parameters predicted for the matrix with ROSETTA using the particle-size distribution shown in Table 3 along with the MLT-derived image variables of the horizons in this study are shown in Table 4. The image variables and predicted K_{sm} were used to calculate a transient saturated hydraulic conductivity of the whole soil following Equation 21. To compare the predictions of K_s from the model in this study to the model proposed by Stewart, Abou Najm, et al. (2016), we fit Equation 48 to the soil shrinkage data determined in this work (Figure 9). The fits described the overall trends in these data reasonably well with predicted ϕ_m values explaining between 84% and 89% of the variation in measured ϕ_m. The values of the soil shrinkage curve parameters in Equation 48 along with their standard errors and residual standard error of the fits for each horizon are shown in Table 5.

Results of the transient saturated hydraulic conductivity predictions from the two models are shown in Figure 10. In all three horizons, trends in K_s time series from the proposed model match predictions from the Stewart, Abou Najm, et al. (2016) model, although there is variation in the magnitude of the values. The Bt horizon showed the best correspondence between the two models, whereas values from the proposed model in the Ap1 horizon and Btkss2 horizons were on average a half an order of magnitude below or above the Stewartet al. (2016a) model, respectively. Comparatively greater correspondence between the models in all three horizons was observed when the matrix water contents were at their recorded lows over the period of study (Figures 7 and 10).

The overall placement of K_s values predicted from the proposed model in relation to the predictions from the Stewart, Abou Najm, et al. (2016) model are also observed in Figure 11 which shows K_s values of the two models normalized by the respective maximum possible K_s across the full range of normalized gravimetric water content. The approximate minimum and maximum U values for the study period (i.e., corresponding to the θ_m values observed in Figure 7) are 0.44–0.68, 0.51–0.74, and 0.38–0.49 for the Ap1, Bt, and Btkss2 horizons, respectively. In these U ranges, the proposed normalized model K_s predictions for the Ap1 and Btkss2 horizons were below or above those predicted by the Stewart, Abou Najm, et al. (2016) model, respectively, corresponding to the K_s values in Figure 10. However, saturated hydraulic conductivities shown in Figure 10b for the Bt horizon have the predicted values from the proposed model below the model from Stewart, Abou Najm, et al. (2016) while the normalized K_s placement is reversed in Figure 11b. This reversal is because the maximum possible K_s predicted from the Stewart, Abou Najm, et al. (2016) model is higher than that predicted in the proposed model, although, in the range of U values for this horizon, the two normalized K_s values showed very close agreement.

The reason for this higher predicted maximum K_s can be seen in Figure 12 where the Stewart, Abou Najm, et al. (2016) model generally predicts a larger macroporosity than the proposed model across most of the range of water contents except under relatively moist conditions (i.e., the left side of the plot) where both models predict reasonably similar macropore fractions. The results in Figure 12 also suggest that macroporosity predictions from the proposed model are generally more conservative than the Stewart, Abou Najm, et al. (2016) model for drier conditions. Overall, these two independently derived models show predictable responses to matrix water content variability, similar trends across the year, and reasonable agreement in their magnitude especially for the Bt horizon. We note that the model proposed by Stewart, Abou Najm, et al. (2016) was applied only to surface

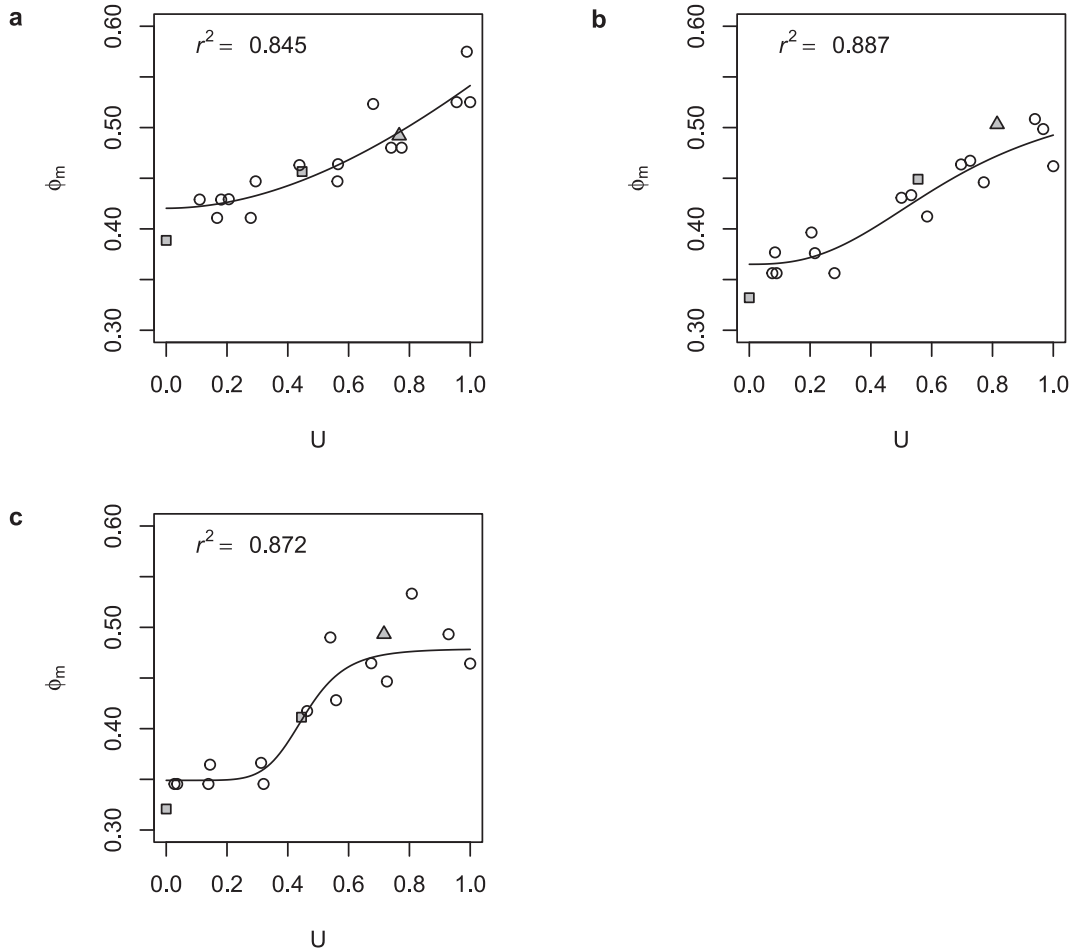

Figure 9. Soil shrinkage curves for the (a) Ap1, (b) Bt, and (c) Btkss2 horizons used in this study showing matrix porosity (ϕ_m) against normalized gravimetric water content $\left(U = \frac{u_m}{u_{\max}}\right)$. Solid lines show the results of the model proposed by Stewart, Rupp, et al. (2016) fit to these data. For reference, shaded squares show the oven-dried and field-capacity bulk density values converted to porosities and along with their respective water contents. Shaded triangles show the location of the saturated water content of the matrix predicted from the ROSETTA pedotransfer function (Schaap et al., 2001) on this curve.

horizons to obtain single transient K_s values for each soil. Thus, one advantage of the proposed model is that it allows a depth-dependent transient K_s to be estimated using quantified macropore images of profile walls (or samples taken from profile walls as is the case in this study).

4.5. Sensitivity of the Model to Measurement Uncertainty

Using a local sensitivity analysis approach, we investigated the impact of measurement error in the static input variables derived from MLT on the calculation of macropore width and saturated hydraulic conductivity

Table 5
Soil Shrinkage Curve Parameters and Residual Standard Errors (RSE) Corresponding to the Fits in Figure 9 for the Function Represented by Equation 48

Horizon	Depth (cm)	p	q	$\phi_{\min}$	$\phi_{\max}$	RSE
Ap1	0–15	0.10 ± 2.83	1.93 ± 3.67	0.420 ± 0.025	0.541 ± 0.016	0.021
Bt	26–47	2.72 ± 6.14	2.63 ± 2.22	0.365 ± 0.014	0.492 ± 0.015	0.016
Btkss2	113–139	196.2 ± 598.8	6.74 ± 3.96	0.349 ± 0.011	0.478 ± 0.013	0.021

Note. Values following ± symbols represent standard errors of the parameters.

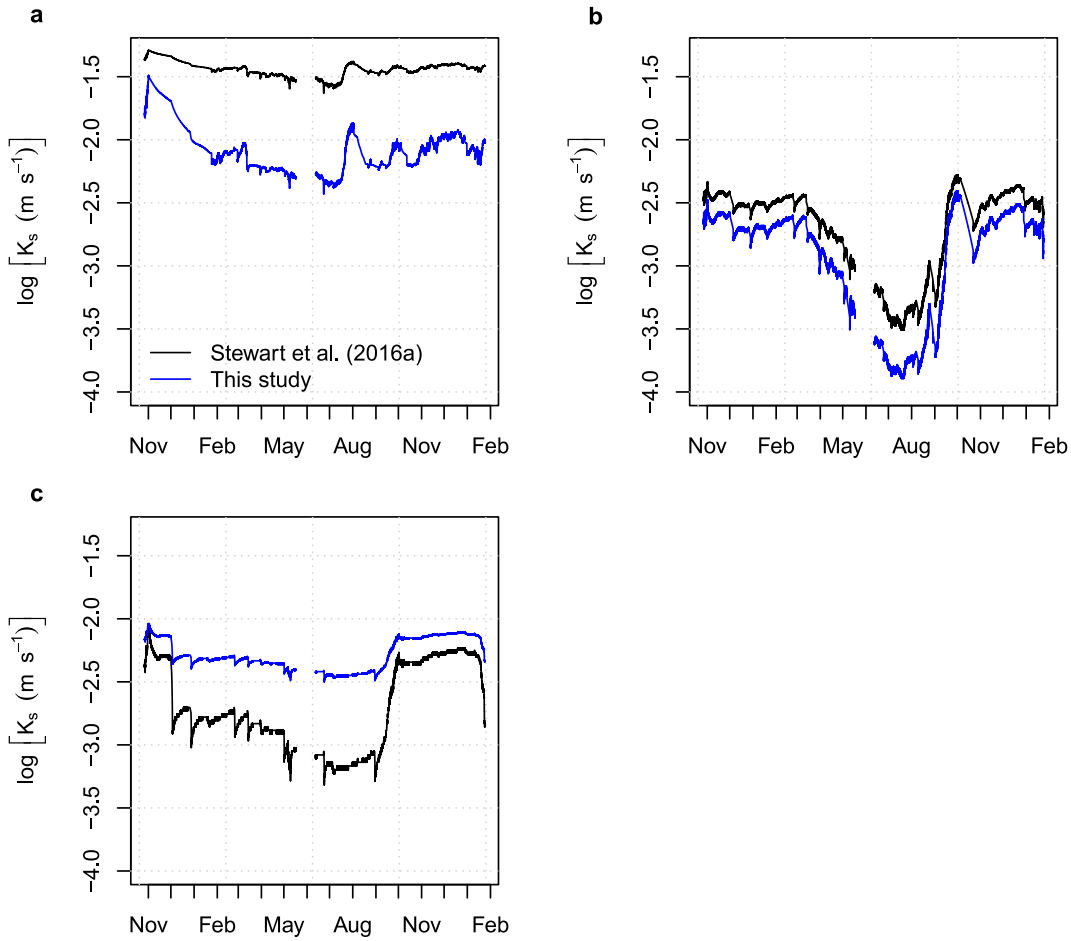

Figure 10. Predicted saturated hydraulic conductivity from the Stewart, Abou Najm, et al. (2016) model and model proposed in this study for the (a) Ap1, (b) Bt, and (c) Btkss2 horizons in the Konza APT soil. Time series shows data between 26 October 2018 and 24 January 2020.

(Figure 13). The three variables considered for one at a time sensitivity analysis were total area of the macropores in the MLT-derived image, total macropore perimeter, and macropore width determined at the scanned moisture state of the sample. These were each varied from their values determined in the Ap1 horizon in this study by ±5% and their effects on the percent change of predicted d and logK_s values were determined across the range of matrix water contents between θ_{wp} and θ_{sm}.

Response surfaces of percent change values for both d and K_s were insensitive to percent relative errors in macropore area determined by MLT across the range of matrix water contents investigated (Figures 13a and 13b). In contrast, d and K_s were significantly sensitive to percent relative errors in macropore perimeter and even more so to dry state macropore width (i.e., above approximately 1%) with decreasing matrix water content (Figures 13c–13f). This is due to the control that P exerts on w_{ds} (Equation 8) and the central role that d_{ds} has in the calculation of $d(\theta_m)$ (Equation 16) which is used, in turn, for the calculation of the conversion factor, R_p (Equation 23), macropore fraction (Equation 22), and, ultimately, K_s (Equation 21). Measurements of P and d_{ds} should, therefore, be accurate to within this relative error range to avoid unrealistic deviations in d or K_s. We are uncertain of the true percent relative error in the measurements determined by MLT; to our knowledge, this analysis has not been performed. However, it is likely that 5% relative error in measurements is far too large of a range to be reasonable. Nonetheless, these response surfaces are illustrative of the direction of change and sensitivity of d and K_s to changes in these MLT input variables.

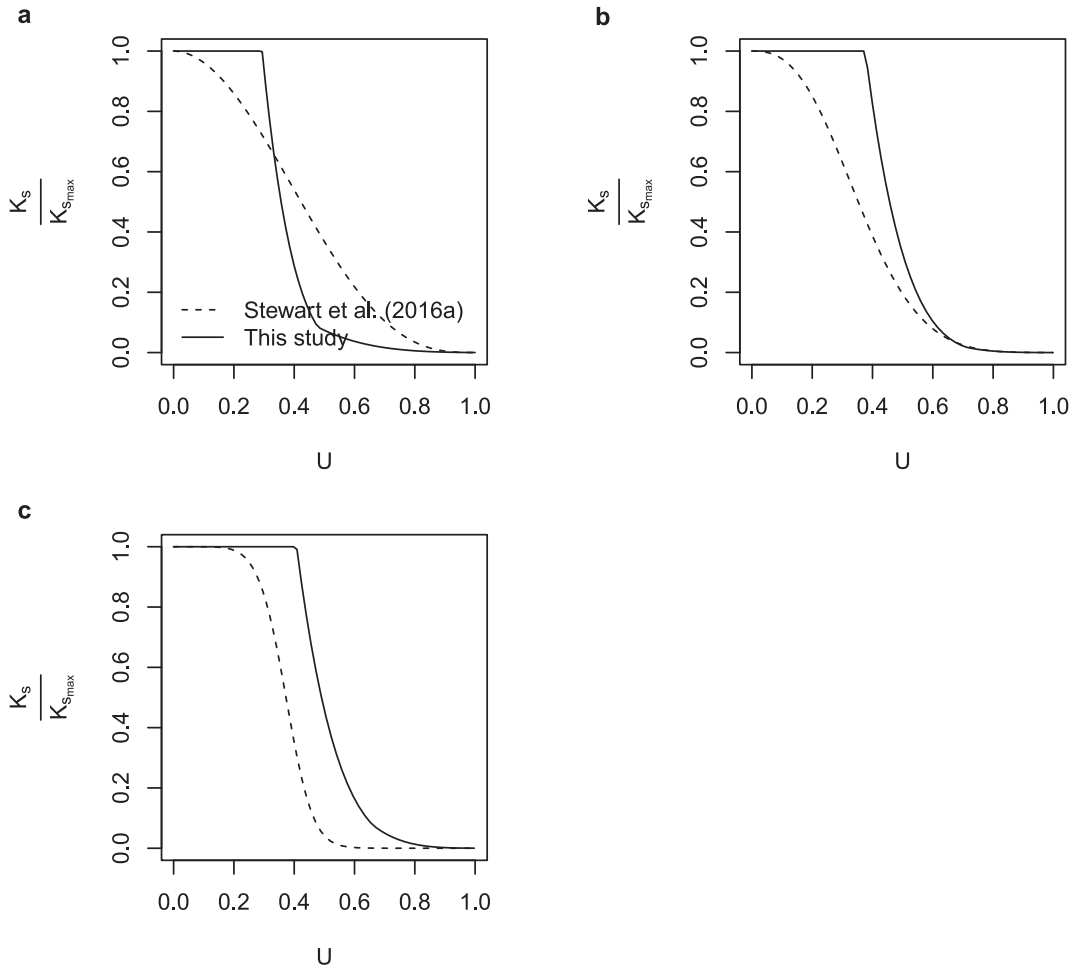

Figure 11. Plots showing the predicted normalized saturated hydraulic conductivity against normalized gravimetric water content for the (a) Ap1, (b) Bt, and (c) Btkss2 horizons in this study using the Stewart, Abou Najm, et al. (2016) model and model proposed in this study.

As discussed in Section 2.1, the theory derived in this work relies on several assumptions including uniformity in the shape (i.e., cubes) and size of structural units within a horizon as well as isotropic shrinkage of those structural units. A necessary consequence of assuming a cubic shape and uniformity in size is that interpedal macropores are conceptualized as straight, smooth, planar slits. Although other models have made similar assumptions (e.g., smooth slits; Chertkov & Ravina, 2001), because real soil interpedal macropores are typically characterized by more complex geometries, the predicted saturated hydraulic conductivity in this model is likely overestimating the true value. For example, macropore angle, tortuosity, and continuity can all contribute to reduce the flow of water in a soil profile (Allaire-Leung et al., 2000; Luo et al., 2010; Saravanathiiban et al., 2014). Additionally, soil shrinkage for well-developed soils is usually greater horizontally than vertically (Hartge & Horn, 2016). Thus, the isotropic shrinkage assumption in this work may underrepresent $d(\theta_m)$ and, thus, the saturated hydraulic conductivity as the soil dries. This is because the d_{ds} determined from the MLT image is averaged to include both vertical and non-vertical macropores, which thus underestimates the true vertical macropore width when thinner non-vertical macropores are included. A decrease in d_{ds} leads to underestimation of transient K_s especially under decreasing matrix water contents (Figures 13e and 13f) in part because only those macropores intersecting a cross section oriented perpendicular to flow are counted in Equations 19 and 20. The degree to which these assumptions, when combined, affect the under or overestimation of K_s should be explored in future work.

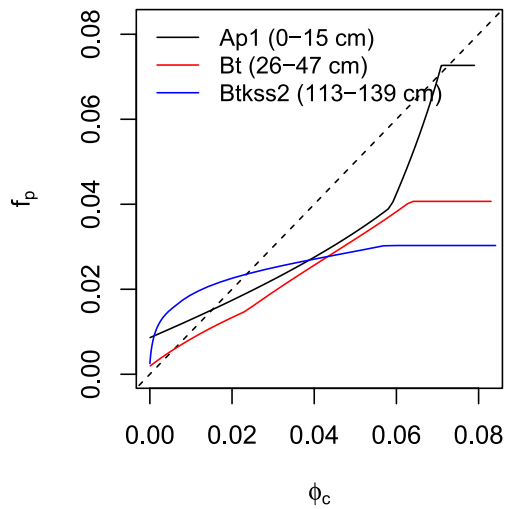

Figure 12. Predicted macropore fraction from this study against macropore porosity predicted by the Stewart, Abou Najm, et al. (2016) model. Dashed line represents the 1:1 relationship between these two predictions.

4.6. Implications of a Transient Saturated Hydraulic Conductivity Term on the Unsaturated Hydraulic Conductivity Function

Figure 14 illustrates the implications of deriving an expression for unsaturated hydraulic conductivity (Equation 38) that depends on the effects of soil matrix water content on macropore water retention and saturated hydraulic conductivity. Here hydraulic conductivity is plotted as a function of the degrees of matrix and macropore saturation. Under conditions where both S_{e_1} and S_{e_2} are at unity, the value represented by the K-surface corresponds to the conventional definition of saturated hydraulic conductivity since all the pores of the soil (i.e., both matrix pores and macropores) are fully saturated with water. We note that it is possible for macropores to be completely closed at the point where the matrix is saturated. In this case, all the pore space is in the matrix, the value of S_{e_2} is undefined, and w_2 is equal to zero.

In the situation where the macropores are drained of water (i.e., $S_{e_2} = 0$), the unsaturated hydraulic conductivity function is described as a single curve that monotonically decreases from K_{sm} as the matrix dries. This is seen where the K-surface intersects the $\log(K)$-S_{e_1} plane at $S_{e_2} = 0$ in Figure 14. However, under conditions when $\theta_m < \theta_{sm}$ and $\theta_p > 0$ (e.g., $S_{e_1} \approx 0$ and $S_{e_2} > 0$), water is present in highly conductive soil macropores that has not yet been absorbed into the matrix; this has the effect of increasing the hydraulic conductivity of the soil even when the soil matrix is extremely dry (and especially so because the macropores are maximally expressed at this moisture state). The intersection of the K-surface with the $\log(K)$-S_{e_2} plane at $S_{e_1} = 1$ represents variably saturated macropore conditions while the soil matrix is saturated. The curve made by the intersection of the K-surface with this plane for the Ap1 horizon (Figure 14a) shows a decrease in conductivity from $\theta_p = f_p$ to 0; this is because macropores are present in this horizon even when $\theta_m = \theta_{sm}$ are increasingly drained in this direction. In contrast, the unsaturated hydraulic conductivity of both the Bt and Btkss2 horizons (Figures 14b and 14c) are constant when the matrix is saturated since macropores are not present at this θ_m (i.e., $\theta_p = f_p = 0$); that is, maximum swelling of the structural units causes macropore width to become negligible in these horizons.

We applied the $K(\theta, \theta_m)$ function to water content data from the horizons in this study (Figure 15). The baseline hydraulic conductivity of the Ap1 horizon over the period of study was lower than the baseline conductivity of the Bt and Btkss2 horizons, although, for several lengthy periods of time throughout the record (e.g., between November 2018 through January 2019 and August to October 2019), the conductivity of the surface was considerably higher than the two subsurface horizons. These periods correspond to relatively dry soil matrix conditions with draining macropore water present likely fed by precipitation (Figure 7). Similarly, the Bt horizon became orders of magnitude more conductive especially during the mid-half of October 2019 after receiving significant inputs of percolating meteoric water following the lowest soil matrix water content on record. In general, the rapid rises (i.e., spikes) in conductivity at the surface is likely fed by precipitation, whereas similar rises in the two subsurface horizons is likely due to inputs of preferential macropore flow to these depths which translate to the high unsaturated hydraulic conductivities predicted from the K-surface in Figure 14. However, the precipitous drop in hydraulic conductivity across all horizons in this study is due to emptying of the macropores either via absorption into the matrix or deeper drainage.

4.7. Comparing Other Approaches to Combining Shrink-Swell Dynamics and Soil Hydraulic Properties

Despite much previous work on the problem, how models of shrink-swell behavior can be combined with models of soil hydraulic properties—specifically, models that account for matrix and macropore domains—to, ultimately, describe soil hydro-mechanical dynamics is still an open question (Barbosa & Gerke, 2024). The approach taken in this study does not directly account for changes in macroporosity due to subsidence, which is similar to models proposed by Chertkov and Ravina (2001) and Coppola et al. (2012, 2015). Coppola et al. (2015) argue that this approximation is reasonable since it is likely to be within the uncertainty of independently determining hydraulic properties for the matrix and macropore domains. However, this assumption means that our model is likely to be more appropriate in soils with well-developed soil structure and shrinkage geometry factors >3 (Coppola et al., 2012; Hartge & Horn, 2016).

10.1029/2024WR039836

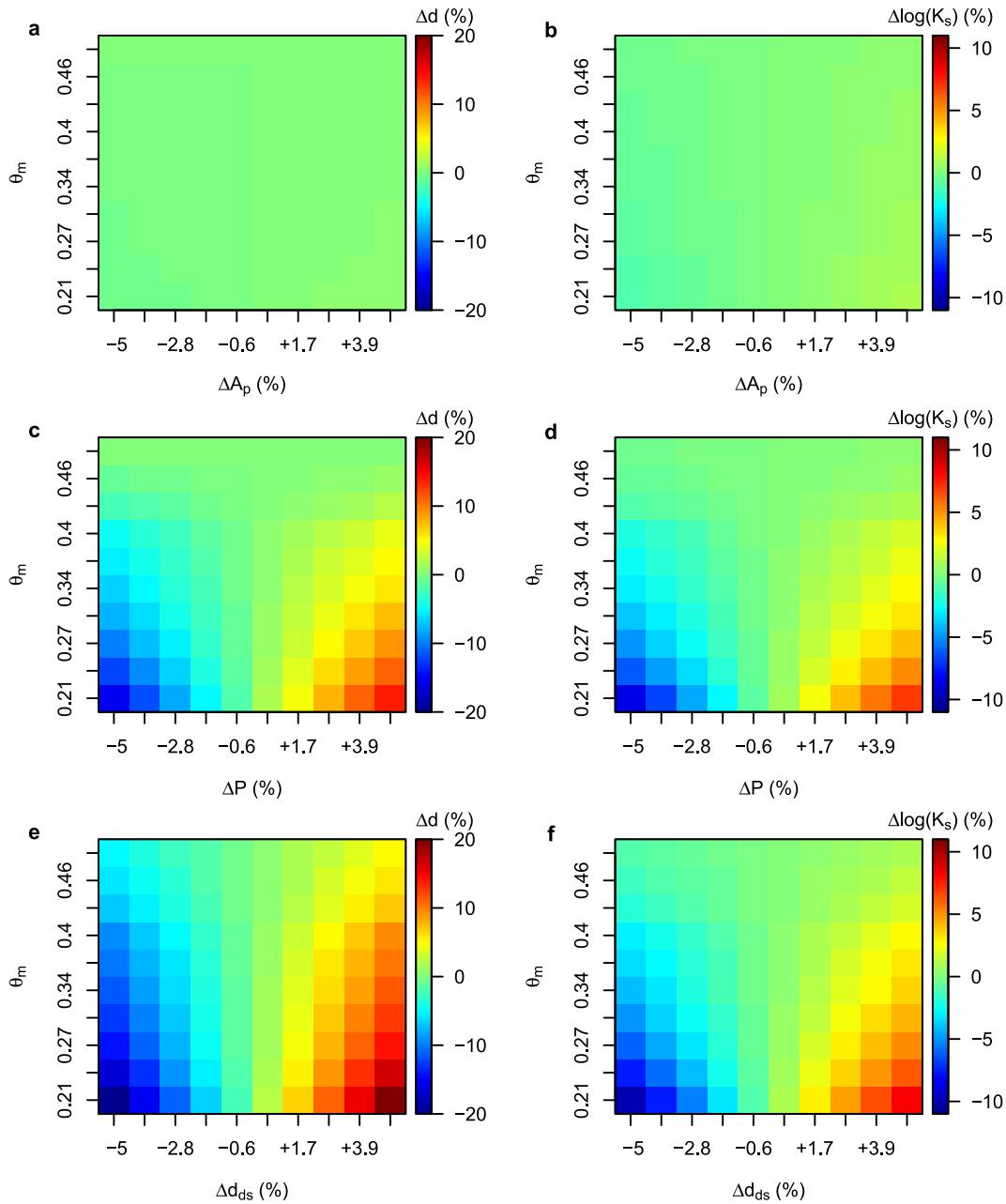

Figure 13. Response of (a, c, e) mean macropore width (d) and (b, d, f) saturated hydraulic conductivity (K_s) to ±5% relative errors in the input variables—(a, b) total pore area (A_p), (c, d) total pore perimeter (P), and (e, f) mean dry-state macropore width (d_{ds})—obtained from the MLT image for the Ap1 horizon of the studied soil.

Similar to Coppola et al. (2012), our model treats the total porosity as constant with the matrix and macropore domains changing as a function of shrinking or swelling in response to changing matrix water contents. However, unlike Chertkov and Ravina (2001), the model does not require that the macropores close at the maximum matrix water content. Changes in macroporosity due to shrink-swell behavior in this model are translated to changes in the macropore domain of a bimodal water retention function (Durner, 1994) similar to other models (e.g., Barbosa & Gerke, 2024; Coppola et al., 2012). Although Barbosa and Gerke (2024) found that structural changes due to shrinking and swelling had a comparatively small effect on the van Genuchten (1980) fitting parameters, we found that shrink-swell behavior had a clear impact on α_2 but not on n_2 and were able to represent the change in α_2 as a function of the ratio of decreasing macropore diameter to the diameter at a dry state (Equation 37). In

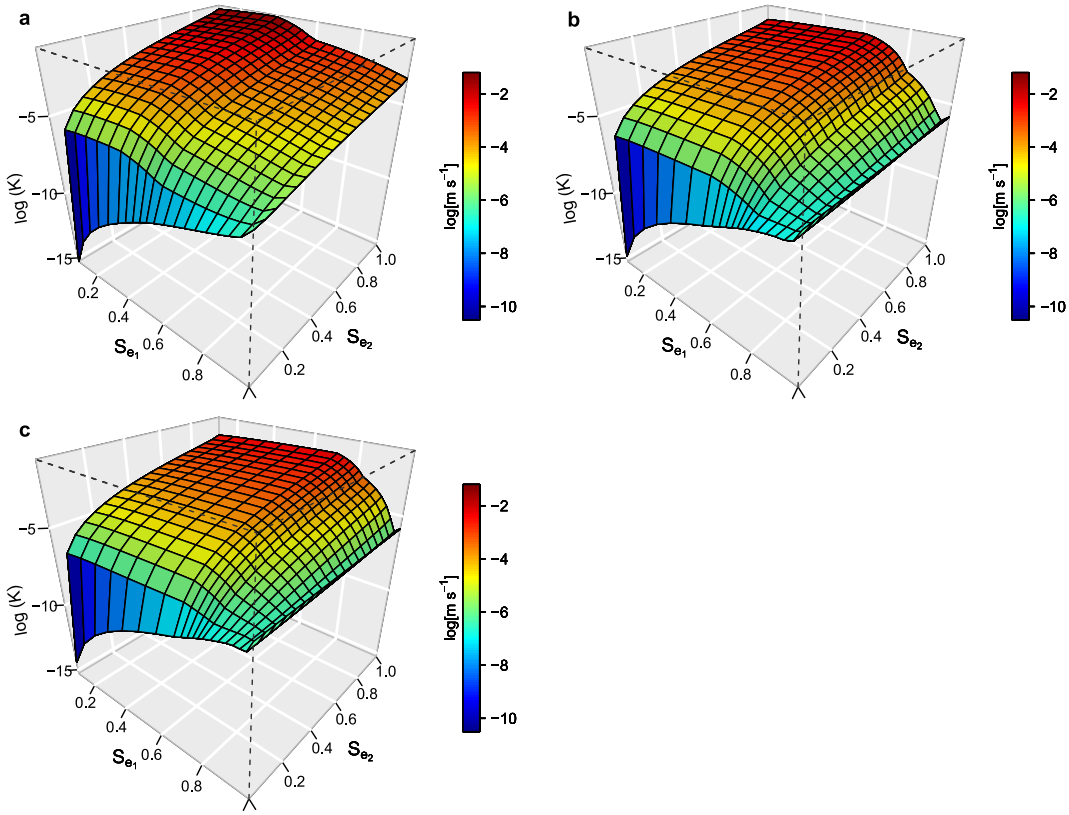

Figure 14. The unsaturated hydraulic conductivity surface for the (a) Ap1 (0–15 cm), (b) Bt (26–47 cm), and (c) Btkss2 (113–139 cm) horizons of the Konza APT soil as a function of degree of saturation of the matrix (S_{e_1}) and macropore (S_{e_2}) domains.

addition, this model considered K_s to be transient similar to Stewart, Abou Najm, et al. (2016), which will change in response to θ_m-induced changes in macroporosity (Barbosa & Gerke, 2024).

An advantage of the model proposed in this work is its reliance on measured macropore data from each horizon. Other models (e.g., Arnold et al., 2005; Bronswijk, 1988a) have required monitoring of changing layer thickness at different depths to calculate macropore volume per unit area necessitating the installation of devices to record

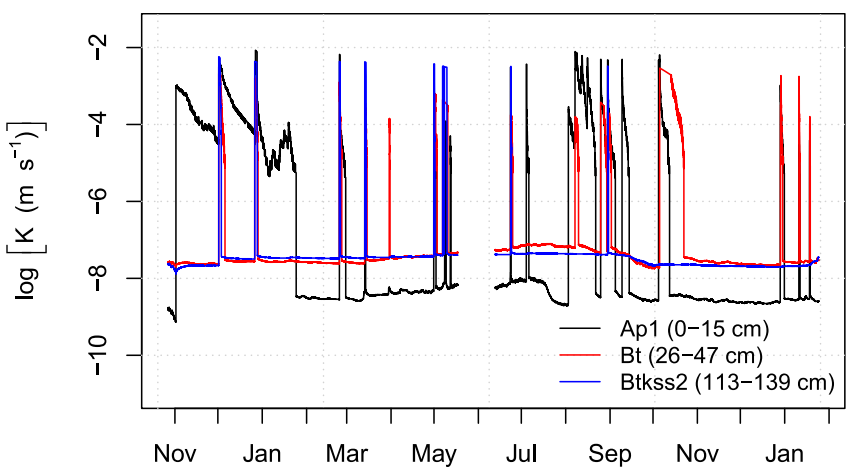

Figure 15. Predicted unsaturated hydraulic conductivity for the Ap1, Bt, and Btkss2 horizons in the Konza APT soil. Time series shows data between 26 October 2018 and 24 January 2020.

these changes (Bronswijk, 1988b). However, our model allows information to be measured at a dry moisture state and related to soil moisture sensor data to predict below ground changes. In addition, the model is unique in that it allows for monitoring change in both soil structural unit and macropore width rather than solely changes in macroporosity. Although other models partition infiltrating meteoric water into macropore and matrix water contents, this has been done using information about crack area at the land surface (Arnold et al., 2005; Bronswijk, 1988a, 1988b; Stewart, Abou Najm, et al., 2016, Stewart, Rupp, et al., 2016) or by modeling the transfer between the macropore and matrix domains as a first order kinetic process (Coppola et al., 2015). In contrast, the theory developed in this study allows macropore and matrix water contents to be separated using peaks in the soil moisture time series independent of soil properties allowing the monitoring of macropore water contents at each sensor depth.

5. Conclusions

In this study, we developed a physically based theory of macropore water retention and saturated and unsaturated hydraulic conductivity that allows MLT-quantified descriptions of macropore geometries from profile cross sections to dynamically respond to sensor-derived soil matrix water content data. In the process of deriving a relationship between macropore width and water content, a method for partitioning total water content into matrix and macropore water contents was developed that was interpretable in terms of profile morphology controlling the hydrologic behavior of the soil. This opens the door to future exploration connecting soil morphological features such as ped-void surface features (e.g., argillans, pressure faces, carbonate coats, redoximorphic accumulations of Fe and Mn on the surface of peds, etc.) directly to the rate at which water is transferred from macropores to the soil matrix. Transient saturated hydraulic conductivity predicted by the model proposed in this work conformed well to K_s predictions from a model previously proposed by Stewart, Abou Najm, et al. (2016). However, the model in this study allows a depth distribution of transient K_s to be predicted because the method relies on cross-sectional images of profile walls.

Although there are advantages to this approach, the reliance on cross-sectional MLT images of macropores is perhaps the biggest limitation to applying the model more broadly. However, other image-based methods (e.g., those that rely on photographs) are expected to work equally well. Future work should evaluate measurement error associated with MLT or other image-based determination of macropore properties given the sensitivity of the predicted macropore width and saturated hydraulic conductivity to significant changes in the perimeter and width of macropores assessed at a dry state. Although the imaging or sampling of intact cross-sections of soil profiles can be labor intensive, the quantitative morphological data obtained by image analysis when combined with soil moisture time series data presents an opportunity to better understand long-term changes to soil structure induced by shifts in climate and land use. Using sensor data from networks such as the National Ecological Observatory Network (NEON) or the US Department of Agriculture–Natural Resources Conservation Service (USDA–NRCS) Soil Climate Analysis Network (SCAN) where bulk density and water content are available is especially salient as it opens the door to connecting structural dynamics to long-term records of soil moisture. If incorporated into future models, Equation 38 could be used to better predict soil hydraulic properties under non-equilbrium flow conditions through macropores. Though the current work focused on a fine-textured mineral soil susceptible to moderate shrink-swell processes, we emphasize that this or a similar approach could be applied to any soil given similar propensity of mineral soil particles, dead organic matter, and living roots to undergo physical changes upon altered water content.

Appendix A: Variable Definitions

Table A1.

Table A1
Definitions and Units of the Variables Used in This Study

Variable	Definition	Units
$\boldsymbol{a}$	Half of the distance by which a macropore is reduced due to the swelling of two adjacent structural units	m
$\boldsymbol{A}$, $\boldsymbol{A_p}$, A_{xs}	Area of the MLT image (i.e., scanned at a dry state) corresponding to the non-macroporous region, macropores (p), and full cross section (xs)	m^2
α_1^{-1}, $\boldsymbol{\alpha_2^{-1}}$, α_{ds}^{-1}	Air-entry potential for the matrix (1) and structural (2) domain and for the structural domain at a dry state (ds)	m
β_0, β_1	Fitting parameters relating $\frac{\alpha_2}{\alpha_{ds}}$ to $\frac{d}{d_{ds}}$	—
C_0, C_1	Empirical parameters relating rod lengths from the method proposed by Schafer and Singer (1976) to *COLE*	—
$\boldsymbol{COLE}$	Coefficient of linear extensibility	—
χ	Shrinkage geometry factor	—
$\boldsymbol{d}$, d_{ds}, $\boldsymbol{d_i}$,	Average macropore width at an arbitrary matrix water content and at a dry state (ds) corresponding to the moisture at which the soil was scanned by MLT; θ_m-adjusted individual macropore widths in the MLT image (i)	m
D	Number of structural macropores per ground area	m^{-2}
δ	*COLE*-correction factor to scale the rate at which the structural unit width changes as a function of matrix water content	—
η	Dynamic viscosity of water	kg m^{-1} s^{-1}
$\boldsymbol{f_p}$, $\boldsymbol{f_{p_i}}$	Total volumetric fraction of macropores (p) and volumetric fraction of individual macropores (p_i)	m^3 m^{-3}
g	Gravitational acceleration	m s^{-2}
γ_0, γ_1, γ_2	Fitting parameters for the model predicting the time derivative of θ_m; values are unitless except for γ_0	s^{-1}
$\boldsymbol{h}$	Matric potential	m
$\boldsymbol{K}$, $\boldsymbol{K_s}$, K_{sm}, $\boldsymbol{K_{sp}}$, K_{cmax}	Hydraulic conductivity at an unsaturated and saturated state (s) for the whole soil; saturated hydraulic conductivity for the matrix (sm) and macropores (sp); maximum crack (macropore) saturated hydraulic conductivity ($cmax$) in the (Stewart, Abou Najm, et al., 2016) model	m s^{-1}
l	Pore connectivity parameter	—
l_s, l_T	Side length (s) of the square-equivalent cross-sectional area and total length (T) representing the boundaries of the structural units in the MLT-scanned cross section	m
m_1, $\boldsymbol{m_2}$	Durner (1994) water retention function fitting parameters corresponding to the matrix (1) and structural (2) domain; assumed to be equal to $1 - \frac{1}{n_i}$ where i is either 1 or 2 corresponding to m_1 and m_2, respectively	—
n_1, n_2, n_{ds}	Durner (1994) water retention function fitting parameter corresponding to the matrix (1) and structural (2) domain and for the structural domain at a dry state (ds)	—
N_s, N_l	Number of squares (s) and lines (l) along a linear transect between two parallel sides of the square equivalent-area cross section	—
p, q	Fitting parameters of the Stewart, Rupp, et al. (2016) soil shrinkage curve	—
P	Total perimeter of the macropores obtained from the MLT image	m
$\boldsymbol{\phi}$, $\boldsymbol{\phi_m}$, $\boldsymbol{\phi_c}$, $\boldsymbol{\phi_b}$, $\phi_{\min}$, $\phi_{\max}$	Total soil and matrix (m) porosity; crack (c), subsidence (b), combined crack and subsidence (cb), minimum matrix (min), and total soil (max) porosities calculated from the Stewart, Abou Najm, et al. (2016) model	m^3 m^{-3}
$\boldsymbol{Q}$	Laminar volumetric flow through a vertical planar macropore	m^3 s^{-1}
$\boldsymbol{r_i}$, r_f	Rod length determined at the ith time step (i) and final rod length (f) after drying	m
$\boldsymbol{R_p}$, $\boldsymbol{R_{p_i}}$	Ratio of the volumetric fraction to areal fraction of macropores corresponding to all (p) or individual (p_i) macropores in the MLT scanned image	—

Table A1
Continued

Variable	Definition	Units
$\boldsymbol{\rho}, \rho_{fc}, \rho_{od}, \rho_s, \rho_w, \rho_p$	Bulk soil density of the matrix, bulk soil density at a field-capacity (fc) and oven-dried (od; i.e., 105°C) state, matrix-saturated bulk soil density (s), water density (w), and particle density (p)	kg m^{-3}
$\boldsymbol{S_{e_1}}, \boldsymbol{S_{e_2}}$	Effective soil water saturation of the matrix (1) and structural macropore (2) domains	—
σ	Surface tension of water	kg s^{-2}
t, Δt	Time corresponding to the collected soil water content data and the time step between contiguous observations	s
$\boldsymbol{\theta}, \boldsymbol{\theta_m}, \boldsymbol{\theta_p}, \boldsymbol{\theta_s}$, θ_{sm} θ_{fc}, θ_r, θ_{wp}, θ_0, θ_1, θ_{pk}, $\Delta\theta$	Volumetric water content of the whole soil, matrix (m), and macropore fraction (p); volumetric water content at a saturated (s) state for the whole soil and field-capacity (fc), residual (r), and wilting point (wp) state for the matrix; antecedent (0), final (1), and peak (pk) volumetric water contents associated with a preferential flow event; change in total water content largely due to the addition of water through macropores	m^3 m^{-3}
$\hat{\boldsymbol{\theta}}_{p_i}, \bar{\boldsymbol{\theta}}_p$	Predicted (ˆ) and mean (¯) matrix water content-adjusted macropore water content	m^3 m^{-3}
$\boldsymbol{u_m}, \boldsymbol{u_{m_i}}$, $u_{\max}$	Gravimetric water content of the matrix (m) and of the rod at the ith time step (m_i) in the determination of *COLE*; maximum (saturated) gravimetric water content of the matrix (max)	kg kg^{-1}
$\boldsymbol{U}$	Maximum-normalized matrix gravimetric water content	—
$\boldsymbol{w}$, w_{ds}	Average structural unit width at an arbitrary matrix water content and at a dry state (ds) corresponding to the moisture at which the soil was scanned by MLT	m
$\hat{\boldsymbol{w}}$	Uncorrected *COLE*-predicted average structural unit width	m
$\boldsymbol{w_1}, \boldsymbol{w_2}$	Weighting factor for the matrix (1) and structural (2) domain in the Durner (1994) unsaturated hydraulic conductivity function	—
W	Combined width of the average structural unit and associated macropores at a dry state corresponding to the moisture at which the soil was scanned by MLT	m

Note. Bolded symbols indicate dynamic (i.e., time-dependent) variables.

Appendix B: Derivation of Macropore Area to Volume Conversion Factor

The ratio of macropore volume fraction to macropore area fraction (R_p; Equation 23) in the MLT-scanned cross section can be derived as follows. First, the soil particles are assumed to be contained in structural units that are distributed within the volume of a soil horizon as packed cubes where adjacent structural units are separated by an average distance d. In this representation, the total volume of each structural unit and its corresponding macropores (V_T) can be calculated as:

$$V_T = (w + d)^3 \tag{B1}$$

The volume of the macropores associated with each structural unit (V_p) is calculated as the difference between the total volume and the volume of just the structural unit:

$$V_p = (w + d)^3 - w^3 \tag{B2}$$

Thus, the volumetric fraction of macropores, f_p, represented by Equation 22 can be expressed as the ratio of V_p to V_T.

The area of each structural unit and its corresponding macropores (A_T) in a vertical cross section is calculated as:

$$A_T = (w + d)^2 \tag{B3}$$

and the area of just the macropores calculated as $d^2 + 2dw$. The areal fraction of macropores in the cross section can also be represented as the ratio of the total area of the macropores in the cross section to the area of that cross section to yield:

$$\frac{A_p}{A_{xs}} = \frac{d^2 + 2dw}{(w+d)^2} \tag{B4}$$

The ratio of f_p to the macropore areal fraction is then given as (Equation 23):

$$R_p = \frac{f_p A_{xs}}{A_p} = \frac{(w+d)^3 - w^3}{(w+d)d(2w+d)} \tag{B5}$$

Within a cross section, macropores occur in a range of widths and areas which are each uniquely quantified in the MLT scan. Each of these macropore widths and areas are reduced from their values at the scanned dry state for values of θ_m above this state. By contrast, the widths of the structural units are conceptualized to be constant for all structural units in the scanned cross section and equivalent to the average width corresponding to θ_m. Thus, the w in Equation B5 is constant for a given value of θ_m whereas d must be computed for each ith macropore width in the image. Hence:

$$R_{p_i} = \frac{(w+d_i)^3 - w^3}{(w+d_i)\,d_i(2w+d_i)} \tag{B6}$$

which is identical to Equation 35.

Data Availability Statement

Daily precipitation data for the KPBS, volumetric water content, macropore, bulk density, water retention, and summary MLT image data for the Ap1, Bt, and Btkss2 horizon from the Konza APT soil, model outputs, and the *R* scripts to generate the figures in this study are available in Dryad (Hirmas et al., 2025) under Creative Commons license CC0 which can be accessed using the following URL: https://doi.org/10.5061/dryad.zs7h44jkn.

Acknowledgments
We thank John Warner and other participating USDA-NRCS soil scientists for help in the field opening, sampling, and describing the soil pit used in this study, the MAPS-EPSCoR team for their sampling efforts, M. Wes Stops for help collecting intact soil monoliths and installing soil sensors, and the USDA-NRCS Kellogg Soil Survey Laboratory staff for their analysis of the collected samples. Dr. Maria Bronnikova, Ben Newcomb, and Vaishnavi Varikuti provided helpful comments on an earlier draft of the manuscript. This work is supported by a Signals in the Soil Grant (HA & DRH - no. 2021-67019-34341; SAB - no. 2021-67019-34338; ANF - no. 2021-67019-34340) from the USDA National Institute of Food and Agriculture and by the National Science Foundation under Grant 2034214 (LL), 2034232 (PLS), 2121760 (HA & DRH), 2121639 (SAB), 2121621 (LL), 2121595 (ANF), 2121694 (PLS), and 1656006 (SAB) with matching support from the State of Kansas through the Kansas Board of Regents. Any opinions, findings, and conclusions or recommendations expressed in this material are those of the authors and do not necessarily reflect the views of the National Science Foundation.

References

Allaire-Leung, S., Gupta, S., & Moncrief, J. (2000). Water and solute movement in soil as influenced by macropore characteristics: 2. Macropore tortuosity. *Journal of Contaminant Hydrology*, *41*(3), 303–315. https://doi.org/10.1016/S0169-7722(99)00074-1

Amer, A.-M. M., Logsdon, S. D., & Davis, D. (2009). Prediction of hydraulic conductivity as related to pore size distribution in unsaturated soils. *Soil Science*, *174*(9), 508–515. https://doi.org/10.1097/SS.0b013e3181b76c29

Arnold, J. G., Potter, K. N., King, K. W., & Allen, P. M. (2005). Estimation of soil cracking and the effect on surface runoff in a Texas blackland prairie watershed. *Hydrological Processes*, *19*(3), 589–603. https://doi.org/10.1002/hyp.5609

Arora, B., Mohanty, B. P., & McGuire, J. T. (2011). Inverse estimation of parameters for multidomain flow models in soil columns with different macropore densities. *Water Resources Research*, *47*(4), W04512. https://doi.org/10.1029/2010WR009451

Bagnall, D. K., Jones, E. J., Balke, S., Morgan, C. L. S., & McBratney, A. B. (2020). An in situ method for quantifying tillage effects on soil structure using multistripe laser triangulation. *Geoderma*, *380*, 114642. https://doi.org/10.1016/j.geoderma.2020.114642

Barbosa, L. A. P., & Gerke, H. H. (2024). Coupled hydro-mechanical pore-scale modeling of biopore-coated clods for upscaling soil shrinkage and hydraulic properties. *Vadose Zone Journal*, *23*(4), e20325. https://doi.org/10.1002/vzj2.20325

Beven, K., & Germann, P. (1982). Macropores and water flow in soils. *Water Resources Research*, *18*, 1311–1325. https://doi.org/10.1002/wrcr.20156

Bird, R., Stewart, W., & Lightfoot, E. (1960). *Transport phenomena*. John Wiley & Sons.

Borchers, H. W. (2023). pracma: Practical numerical math functions (R package version 2.4.4) [Computer software manual]. Retrieved from https://CRAN.R-project.org/package=pracma

Bordoloi, S., Ni, J., & Ng, C. W. W. (2020). Soil desiccation cracking and its characterization in vegetated soil: A perspective review. *Science of the Total Environment*, *729*, 138760. https://doi.org/10.1016/j.scitotenv.2020.138760

Bronswijk, J. (1988a). Effect of swelling and shrinkage on the calculation of water balance and water transport in clay soils. *Agricultural Water Management*, *14*(1), 185–193. (Agrohydrology—Recent Developments). https://doi.org/10.1016/0378-3774(88)90073-X

Bronswijk, J. (1988b). Modeling of water balance, cracking and subsidence of clay soils. *Journal of Hydrology*, *97*(3), 199–212. https://doi.org/10.1016/0022-1694(88)90115-1

Brutsaert, W., & Nieber, J. L. (1977). Regionalized drought flow hydrographs from a mature glaciated plateau. *Water Resources Research*, *13*(3), 637–643. https://doi.org/10.1029/WR013i003p00637

Caplan, J. S., Gimenez, D., Hirmas, D. R., Brunsell, N. A., Blair, J. M., & Knapp, A. K. (2019). Decadal-scale shifts in soil hydraulic properties as induced by altered precipitation. *Science Advances*, *5*(9), eaau6635. https://doi.org/10.1126/sciadv.aau6635

Chertkov, V. Y., & Ravina, I. (2001). Effect of interaggregate capillary cracks on the hydraulic conductivity of swelling clay soils. *Water Resources Research*, *37*(5), 1245–1256. https://doi.org/10.1029/2000WR900319

Coppola, A., Comegna, A., Dragonetti, G., Gerke, H. H., & Basile, A. (2015). Simulated preferential water flow and solute transport in shrinking soils. *Vadose Zone Journal*, *14*(9), 1–22. https://doi.org/10.2136/vzj2015.02.0021

Coppola, A., Gerke, H. H., Comegna, A., Basile, A., & Comegna, V. (2012). Dual-permeability model for flow in shrinking soil with dominant horizontal deformation. *Water Resources Research*, *48*(8). https://doi.org/10.1029/2011WR011376

Dauer, J. M., Withington, J. M., Oleksyn, J., Chorover, J., Chadwick, O. A., Reich, P. B., & Eissenstat, D. M. (2009). A scanner-based approach to soil profile-wall mapping of root distribution. *Dendrobiology*, *62*, 35–40.
Dexter, A. (2004). Soil physical quality—Part I. Theory, effects of soil texture, density, and organic matter, and effects on root growth. *Geoderma*, *120*(3–4), 201–214. https://doi.org/10.1016/j.geoderma.2003.09.004
Drager, K. I., Hirmas, D. R., Hasiotis, S. T., & Bents, T. C. (2016). Effects of ant (*Formica subsericea*) nest development on physical and hydrological properties in a coarse-textured soil. *Soil Science*, *181*(3–4), 166–174. https://doi.org/10.1097/SS.0000000000000145
Dralle, D. N., Karst, N. J., Charalampous, K., Veenstra, A., & Thompson, S. E. (2017). Event-scale power law recession analysis: Quantifying methodological uncertainty. *Hydrology and Earth System Sciences*, *21*(1), 65–81. https://doi.org/10.5194/hess-21-65-2017
Durner, W. (1994). Hydraulic conductivity estimation for soils with heterogenous pore structure. *Water Resources Research*, *30*(2), 211–223. https://doi.org/10.1029/93WR02676
Eck, D. V., Hirmas, D. R., & Giménez, D. (2013). Quantifying soil structure from field excavation walls using multistripe laser triangulation scanning. *Soil Science Society of America Journal*, *77*(4), 1319–1328. https://doi.org/10.2136/sssaj2012.0421
Eck, D. V., Qin, M., Hirmas, D. R., Giménez, D., & Brunsell, N. A. (2016). Relating quantitative soil structure metrics to saturated hydraulic conductivity. *Vadose Zone Journal*, *15*(1), 1–11. https://doi.org/10.2136/vzj2015.05.0083
Hartemink, A. E., & Minasny, B. (2014). Towards digital soil morphometrics. *Geoderma*, *230*, 305–317. https://doi.org/10.1016/j.geoderma.2014.03.008
Hartge, K. H., & Horn, R. (2016). In R. Horton, R. Horn, J. Bachmann, & S. Peth (Eds.), *Essential soil physics*. Schweizerbart Science Publishers.
Hillel, D. (1998). *Environmental soil physics*. Academic Press.
Hirmas, D. R. (2013). A simple method for removing artifacts from moist fine-textured soil faces. *Soil Science Society of America Journal*, *77*(2), 591–593. https://doi.org/10.2136/sssaj2012.0418n
Hirmas, D. R., Ajami, H., Sena, M. G., Zhang, X., Cao, X., Li, B., et al. (2025). Predicting soil interpedal macroporosity and hydraulic conductivity dynamics: A model for integrating laser-scanned profile imagery with soil moisture sensor data [Dataset]. *Dryad*. https://doi.org/10.5061/dryad.zs7h44jkn
Hirmas, D. R., Giménez, D., Mome Filho, E. A., Patterson, M., Drager, K., Platt, B. F., & Eck, D. V. (2016). Quantifying soil structure and porosity using three-dimensional laser scanning. In A. Hartemink & B. Minasny (Eds.), *Digital soil morphometrics* (pp. 19–35). https://doi.org/10.1007/978-3-319-28295-4_2
Hobley, E., Steffens, M., Bauke, S. L., & Koegel-Knabner, I. (2018). Hotspots of soil organic carbon storage revealed by laboratory hyperspectral imaging. *Scientific Reports*, *8*(1), 13900. https://doi.org/10.1038/s41598-018-31776-w
Hunt, A. G., Ewing, R. P., & Horton, R. (2013). What's wrong with soil physics? *Soil Science Society of America Journal*, *77*(6), 1877–1887. https://doi.org/10.2136/sssaj2013.01.0020
Jarvis, N. J. (2007). A review of non-equilibrium water flow and solute transport in soil macropores: Principles, controlling factors and consequences for water quality. *European Journal of Soil Science*, *58*(3), 523–546. https://doi.org/10.1111/j.1365-2389.2007.00915.x
Kirchner, J. W. (2009). Catchments as simple dynamical systems: Catchment characterization, rainfall-runoff modeling, and doing hydrology backward. *Water Resources Research*, *45*(2), W02429. https://doi.org/10.1029/2008WR006912
Lepore, B. J., Morgan, C. L. S., Norman, J. M., & Molling, C. C. (2009). A mesopore and matrix infiltration model based on soil structure. *Geoderma*, *152*(3–4), 301–313. https://doi.org/10.1016/j.geoderma.2009.06.016
Lewandowska, J., Szymkiewicz, A., Gorczewska, W., & Vauclin, M. (2005). Infiltration in a double-porosity medium: Experiments and comparison with a theoretical model. *Water Resources Research*, *41*(2), W02022. https://doi.org/10.1029/2004WR003504
Luo, L., Lin, H., & Schmidt, J. (2010). Quantitative relationships between soil macropore characteristics and preferential flow and transport. *Soil Science Society of America Journal*, *74*(6), 1929–1937. https://doi.org/10.2136/sssaj2010.0062
Maechler, M., Rousseeuw, P., Croux, C., Todorov, V., Ruckstuhl, A., Salibian-Barrera, M., et al. (2024). robustbase: Basic robust statistics (R package version 0.99-2) [Computer software manual]. Retrieved from http://robustbase.r-forge.r-project.org/
Mualem, Y. (1976). New model for predicting hydraulic conductivity of unsaturated porous-media. *Water Resources Research*, *12*(3), 513–522. https://doi.org/10.1029/WR012i003p00513
Nash, J., & Sutcliffe, J. (1970). River flow forecasting through conceptual models part I — A discussion of principles. *Journal of Hydrology*, *10*(3), 282–290. https://doi.org/10.1016/0022-1694(70)90255-6
National Cooperative Soil Survey. (2025). NCSS soil characterization database (lab data Mart). Retrieved from https://www.nrcs.usda.gov/resources/data-and-reports/ncss-soil-characterization-data-lab-data-mart. Accessed: 2025-06-15.
Peng, X., & Horn, R. (2005). Modeling soil shrinkage curve across a wide range of soil types. *Soil Science Society of America Journal*, *69*(3), 584–592. https://doi.org/10.2136/sssaj2004.0146
Radcliffe, D., & Šimůnek, J. (2010). *Soil physics with Hydrus: Modeling and applications*. CRC Press.
R Core Team. (2024). R: A language and environment for statistical computing [Computer software manual]. Retrieved from https://www.R-project.org/
Saravanathiiban, D. S., Kutay, M. E., & Khire, M. V. (2014). Effect of macropore tortuosity and morphology on preferential flow through saturated soil: A lattice Boltzmann study. *Computers and Geotechnics*, *59*, 44–53. https://doi.org/10.1016/j.compgeo.2014.02.006
Schaap, M. G., Leij, F. J., & van Genuchten, M. T. (2001). Rosetta: A computer program for estimating soil hydraulic parameters with hierarchical pedotransfer functions. *Journal of Hydrology*, *251*(3–4), 163–176. https://doi.org/10.1016/S0022-1694(01)00466-8
Schafer, W. M., & Singer, M. J. (1976). New method of measuring shrink-swell potential using soil pastes. *Soil Science Society of America Journal*, *40*(5), 805–806. https://doi.org/10.2136/sssaj1976.03615995004000050050x
Schneider, C. A., Rasband, W. S., & Eliceiri, K. W. (2012). NIH image to ImageJ: 25 years of image analysis. *Nature Methods*, *9*(7), 671–675. https://doi.org/10.1038/nmeth.2089
Šimůnek, J., & van Genuchten, M. T. (2008). Modeling nonequilibrium flow and transport processes using Hydrus. *Vadose Zone Journal*, *7*(2), 782–797. https://doi.org/10.2136/vzj2007.0074
Slette, I. J., Blair, J. M., Fay, P. A., Smith, M. D., & Knapp, A. K. (2022). Effects of compounded precipitation pattern intensification and drought occur belowground in a mesic grassland. *Ecosystems*, *25*(6), 1265–1278. https://doi.org/10.1007/s10021-021-00714-9
Soil Science Division Staff. (2017). In C. Ditzler, K. Scheffe, & H. Monger (Eds.), *Soil survey manual. USDA Handbook 18*. Department of Agriculture, Government Printing Office.
Soil Survey Staff. (2014). Kellogg soil Survey laboratory methods manual. Soil Survey investigations report No. 42, version 5.0 (R. Burt & soil Survey staff). In *Natural Resources conservation Service*. U.S. Department of Agriculture.
Stewart, R. D., Abou Najm, M. R., Rupp, D. E., & Selker, J. S. (2016). Modeling multidomain hydraulic properties of shrink-swell soils. *Water Resources Research*, *52*(10), 7911–7930. https://doi.org/10.1002/2016WR019336

Stewart, R. D., Rupp, D. E., Abou Najm, M. R., & Selker, J. S. (2016). A unified model for soil shrinkage, subsidence, and cracking. *Vadose Zone Journal*, *15*(3), 1–15. https://doi.org/10.2136/vzj2015.11.0146

van Genuchten, M. T. (1980). A closed-form equation for predicting the hydraulic conductivity of unsaturated soils. *Soil Science Society of America Journal*, *44*(5), 892–898. https://doi.org/10.2136/sssaj1980.03615995004400050002x

Watson, K. W., & Luxmoore, R. J. (1986). Estimating macroporosity in a forest watershed by use of a tension infiltrometer. *Soil Science Society of America Journal*, *50*(3), 578–582. https://doi.org/10.2136/sssaj1986.03615995005000030007x

Xu, S., Wang, M., Shi, X., Yu, Q., & Zhang, Z. (2021). Integrating hyperspectral imaging with machine learning techniques for the high-resolution mapping of soil nitrogen fractions in soil profiles. *Science of the Total Environment*, *754*, 142135. https://doi.org/10.1016/j.scitotenv.2020.142135

Zhang, Y., & Hartemink, A. E. (2019). Digital mapping of a soil profile. *European Journal of Soil Science*, *70*(1, SI), 27–41. https://doi.org/10.1111/ejss.12699